Multifaceted Water Dynamics in Spherical Nanocages

Michael von Domaros,[†] Dusan Bratko,[‡] Barbara Kirchner,[¶] Gerhard Hummer,[§] and Alenka Luzar[*,‡]

†*Department of Chemistry, University of California, Irvine, Irvine, CA 92697, USA*
‡*Department of Chemistry, Virginia Commonwealth University, Richmond, VA 23284, USA*
¶*Mulliken Center for Theoretical Chemistry, University of Bonn, 53127 Bonn, Germany*
§*Max Planck Institute of Biophysics, 60438 Frankfurt am Main, Germany*

E-mail: aluzar@vcu.edu

Abstract

We present a new method to study position-dependent, anisotropic diffusion tensors inside spherically confined systems—a geometry that is common to many chemical nanoreactors. We use this method to elucidate the surprisingly rich solvent dynamics of confined water. The spatial variation of the strongly anisotropic diffusion predicted by the model agrees with the results of explicit molecular dynamics simulations. The same approach can be directly transferred to the transport of solutes to and from reaction sites located at nanoreactor interfaces. We complement our study by a detailed analysis of water hydrogen bond kinetics, which is intimately coupled to diffusion. Despite the inhomogeneity in structure and translational dynamics inside our nanocages, a single set of well-defined rate constants is sufficient to accurately describe the kinetics of hydrogen bond breaking and formation. We find that once system size effects have been eliminated, the residence times of water molecules inside the coordination shell of a hydrogen bond partner are well correlated to average diffusion constants obtained from the procedure above.

Introduction

With the continuing trend towards miniaturization, chemical nanoreactors have moved into the focus of contemporary research. In a recent *ACS Select* virtual issue,[1] numerous exciting applications of such systems have been highlighted, ranging from the selective control of molecular interactions within metal-organic frameworks[2] to the promotion of peptide bonding in liposomes.[3] Like in any type of reactor, chemical and transport dynamics of both solutes and solvent play a critical role in reactions taking place at the nanoscale. Here, we present a detailed computational analysis of water dynamics inside *spherical* nanocages, a geometry that is frequently found in chemical nanoreactors[4].

Motivated by the large variation in water–surface interactions and system geometries, several previous studies have already been dedicated to the properties of water inside nanoconfined systems. For example, rapid water flow was observed in narrow carbon nanotubes and other hydrophobic pores, which form low-friction conduits for water transport.[5–9] Furthermore, prolonged hydrogen bond lifetime is associated with that flow in narrow pores, where only small threads of water can pass.[5] Similar results were obtained close to planar hydrophobic interfaces, where parallel diffusion is also exceptionally fast.[10–12] Unlike in narrow confine-

Supporting Information: Multifaceted Water Dynamics in Spherical Nanocages

Michael von Domaros,[†] Dusan Bratko,[‡] Barbara Kirchner,[¶] Gerhard Hummer,[§] and Alenka Luzar[*,‡]

†*Department of Chemistry, University of California, Irvine, Irvine, CA 92697, USA*
‡*Department of Chemistry, Virginia Commonwealth University, Richmond, VA 23284, USA*
¶*Mulliken Center for Theoretical Chemistry, University of Bonn, 53127 Bonn, Germany*
§*Max Planck Institute of Biophysics, 60438 Frankfurt am Main, Germany*

E-mail: aluzar@vcu.edu

Water Network Structure

For the lack of specialized metrics of hydrogen bond structure in anisotropic environments, we rely on hydrogen-bond criteria and a tetrahedral order parameter originally developed for isotropic systems. Similar approximations have proven to yield useful insights into structural properties of hydration water[1] The order parameter we use is split into an angular (S_g) and distance (S_k) part, according to the definition[2] of Chau and Hardwick:

$$S_g = \frac{3}{32} \sum_{j=1}^{3} \sum_{k=j+1}^{4} \left(\cos \Psi_{j,k} + \frac{1}{3} \right)^2 \tag{S1}$$

$$S_k = \frac{1}{3} \sum_{k=1}^{4} \frac{\left(r_k - \hat{r}\right)^2}{4\hat{r}^2} \,. \tag{S2}$$

Therein, the summation indices run over the four closest neighbors of a selected water molecule, $\Psi_{j,k}$ denotes the angle between the central molecule and its neighbors j and k, r_k is the distance to the closest neighbor k, and $\hat{r}$ is the arithmetic mean of the four radial distances. Both values are zero for a perfect tetrahedron, but approach somewhat larger values ($S_g \approx 0.1, S_k \approx 1.3 \times 10^{-3}$) in bulk water at ambient conditions.[2] The parameters are shown in Figures S1 and S2 and their discussion follows shortly.

Hydrogen bonds were detected by the same geometric criterion used in the discussion of hydrogen bond kinetics[3,4] (main article). The ensemble average of the hydrogen bond population operator $\langle h \rangle$ is closely related to the average number of hydrogen bonds per water molecule $\langle n_{\mathrm{hb}} \rangle$, according to

$$\langle n_{\mathrm{hb}} \rangle = \frac{N-1}{2} \langle h \rangle \,. \tag{S3}$$

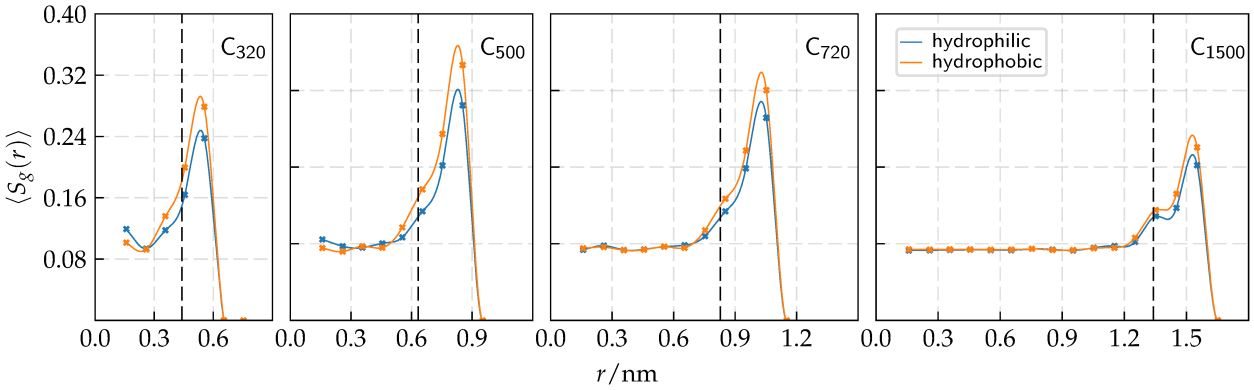

Figure S1: Average angular part $\langle S_g\,(r)\rangle$ of the tetrahedral order parameter[2] as a function of the radial distance r from the nanocage center. Lines are meant to guide the eye. The dashed vertical line indicates the position of the interfacial density maximum.

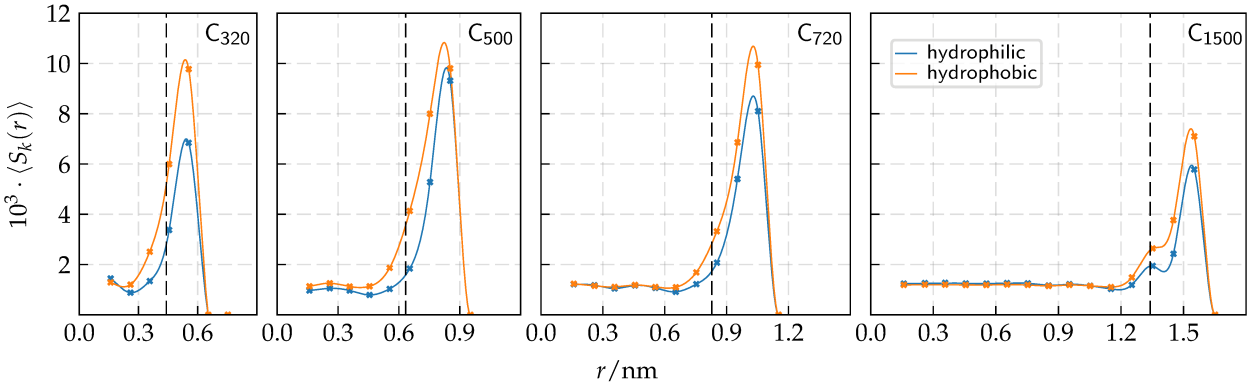

Figure S2: Average of the distance part $\langle S_k\,(r)\rangle$ of the tetrahedral order parameter[2] as a function of the radial distance r from the nanocage center. Lines are meant to guide the eye. The dashed vertical line indicates the position of the interfacial density maximum.

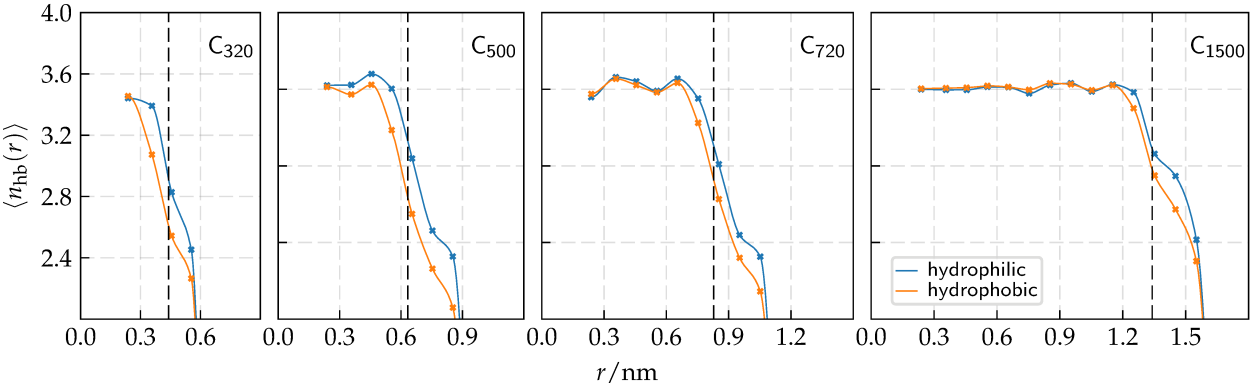

Figure S3: Average number of hydrogen bonds per water molecule $\langle n_{\mathrm{hb}}\,(r)\rangle$ as a function of the radial distance r from the nanocage center. Lines are meant to guide the eye. The dashed vertical line indicates the position of the interfacial density maximum.

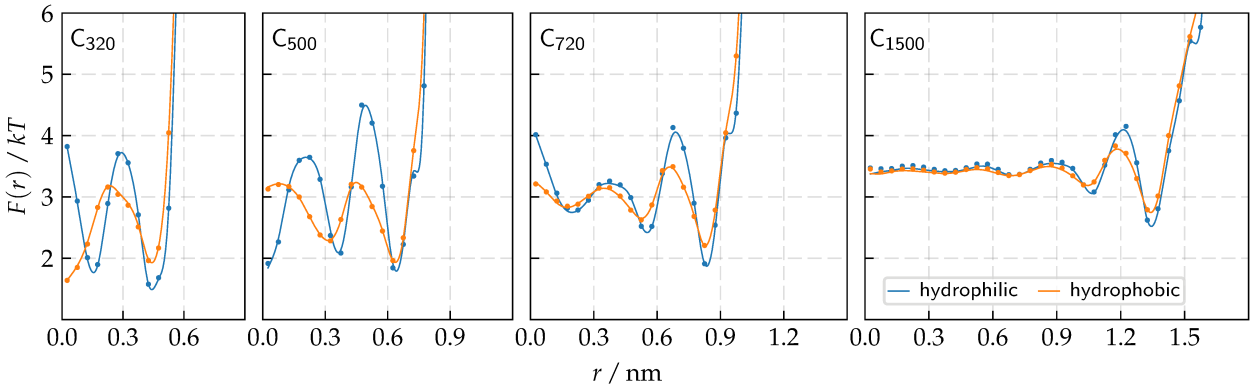

Figure S4: Free energy profiles $F(r)$ as a function of the radial distance r from the nanocage center. Results were obtained from counting statistics (solid lines) and from Bayesian sampling (dots).

Distance dependent profiles of these averages are shown in Figure S3.

The profiles shown in Figures S1–S3 report on the water hydrogen bond network in one way or another, and thus, share a number of common features. In all systems, the interfacial hydrogen bond network is being significantly disturbed by the interface. The average number of hydrogen bonds is almost halved within the outermost water shell, which is accompanied by significant distortion of tetrahedrality. These effects are more pronounced in hydrophobic than in hydrophilic cages. Water molecules that reside away from the outermost water shell are less hindered by the geometric restrictions, as indicated by the plateau values of the various parameters.

Diffusion

Note that free energy profiles are also directly accessible from counting statistics

$$F(r) = -kT \ln p(r), \tag{S4}$$

where $p(r)$ is the local probability density of finding a particle at position r. The preceding equation can be evaluated by discretization and results are shown in comparison to those obtained from the Bayesian sampling procedure in Figure S4. Agreement is perfect, further increasing the confidence in our diffusion models.

The radial and angular propagators $G(r, t|r', 0)$ and $P(r, \cos\theta, t|r', 0)$ corresponding to those in the main text, but in the hydrophilic confinements, are shown in Figure S5. They behave qualitatively as their hydrophobic counterparts.

Furthermore, we show additional angular propagators $P(r, \cos\theta, t|r', 0)$ where r' has been restricted to the outermost radial density minimum $r_{\min}$ (Figure S6). In combination with those propagators shown for the interfacial density maximum, the data shown here and in the main text covers the most critical regions of our systems. Once again, agreement between model and simulation data is less perfect in angular than in radial direction, but still quantitatively convincing.

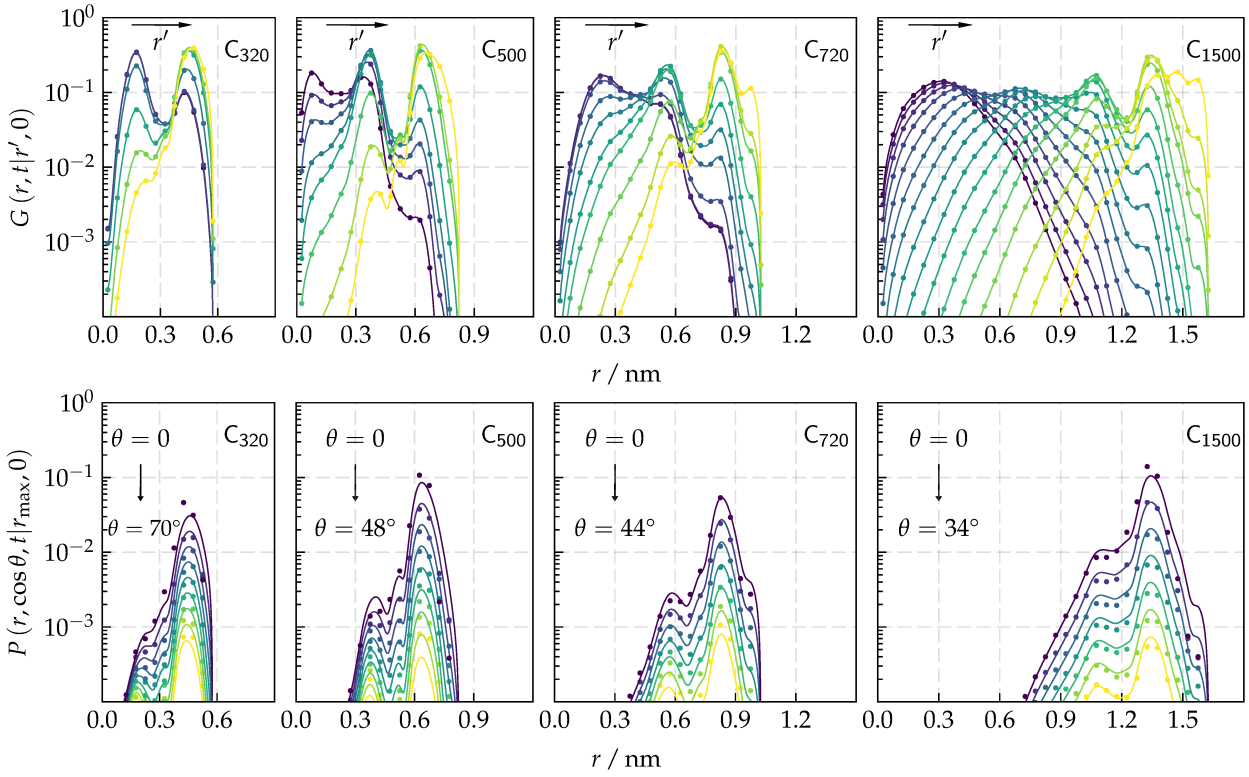

Figure S5: Model propagators (solid lines) in radial and angular direction, $G\,(r,t|r',0)$ and $P\,(r,\cos\theta,t|r',0)$, compared to simulation data (symbols) in the hydrophilic confinements for a lag time of 10 ps. The color gradient indicates increasing initial positions r' and $\cos\theta$, respectively.

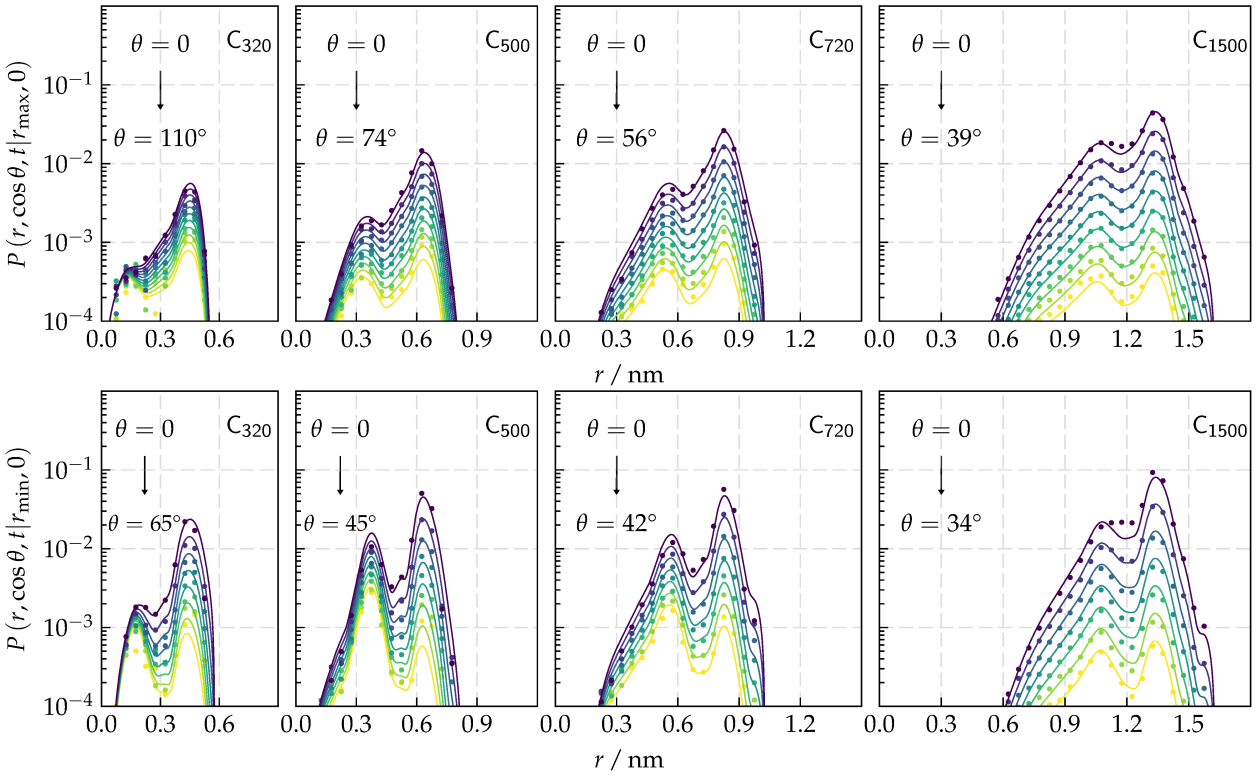

Figure S6: Model propagators $P\,(r, \cos\theta, t|r', 0)$ (solid lines) compared to simulation data (symbols) in the hydrophobic confinements (top) and hydrophilic confinements (bottom) for a lag time of 10 ps. The initial position of the particle has been restricted to the outermost density minimum $r' = r_{\mathrm{min}}$ in this plot. The color gradient indicates decreasing values of $\cos\theta$.

We observe a non-monotonic dependence of the interfacial diffusivities $D_\perp(R_\mathrm{G})$ and $D_\parallel(R_\mathrm{G})$ (Fig. S7), where R_G is the approximate location of the Gibbs dividing surface defined in analogy to ref. 5. Although the curves are reminiscent of those observed at convex interfaces,[5] where the minimum has been explained with the structural crossover length scale for hydrophobic hydration, the underlying mechanisms cannot be the same, since there is no such crossover in our systems.

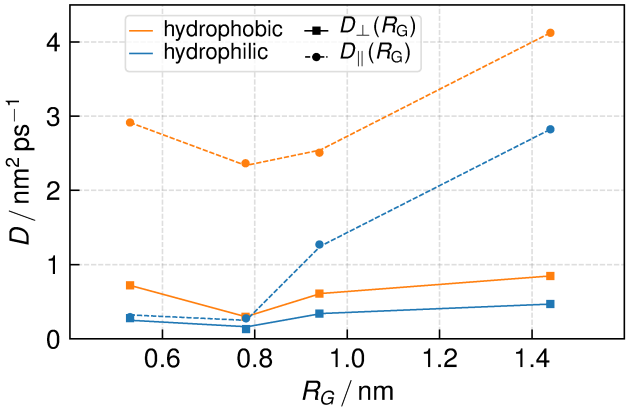

Figure S7: Interfacial diffusivities $D_\perp(R_\mathrm{G})$ and $D_\parallel(R_\mathrm{G})$ at the approximate location of the Gibbs dividing surface (i.e., where $\rho(R_\mathrm{G}) \sim {}^1\!/_2\,\rho_\mathrm{bulk}$). Lines are meant to guide the eye.

Hydrogen Bond Kinetics

Here, we show reactive flux time correlation functions $k(t)$ and $k_\mathrm{in}(t)$, as well as their model predictions, and correlation plots for bulk water (Figure S8), for the hydrophobic confinements (Figure S9), and for the hydrophilic confinements (Figure S10). All parameters required in our analyses are summarized in Table S1. A discussion of these results has been given in the main text.

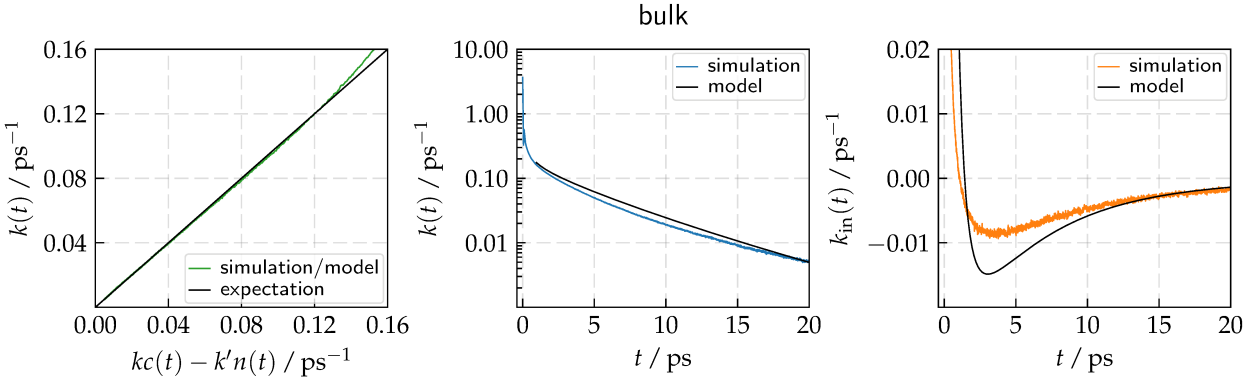

Figure S8: Correlation between the hydrogen bond kinetics phenomenology and simulation data, as well as the reactive flux time correlation functions $k(t)$ and $k_\mathrm{in}(t)$ and their respective model predictions (Equation (6); main text) in bulk SPC/E water.

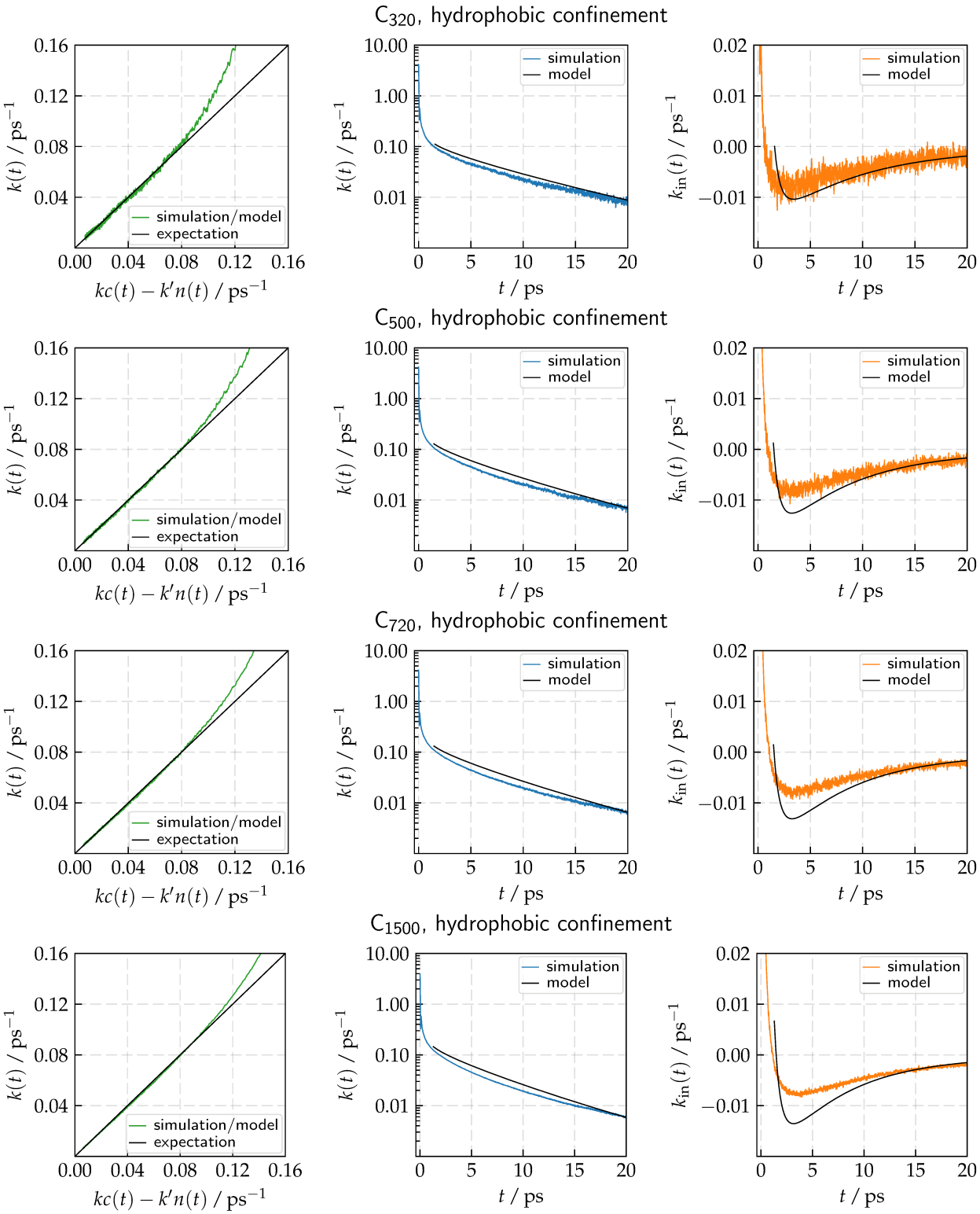

Figure S9: Correlation between the hydrogen bond kinetics phenomenology and simulation data, as well as the reactive flux time correlation functions $k(t)$ and $k_{\mathrm{in}}(t)$ and their respective model predictions (Equation (6); main text) in all hydrophobic confinements.

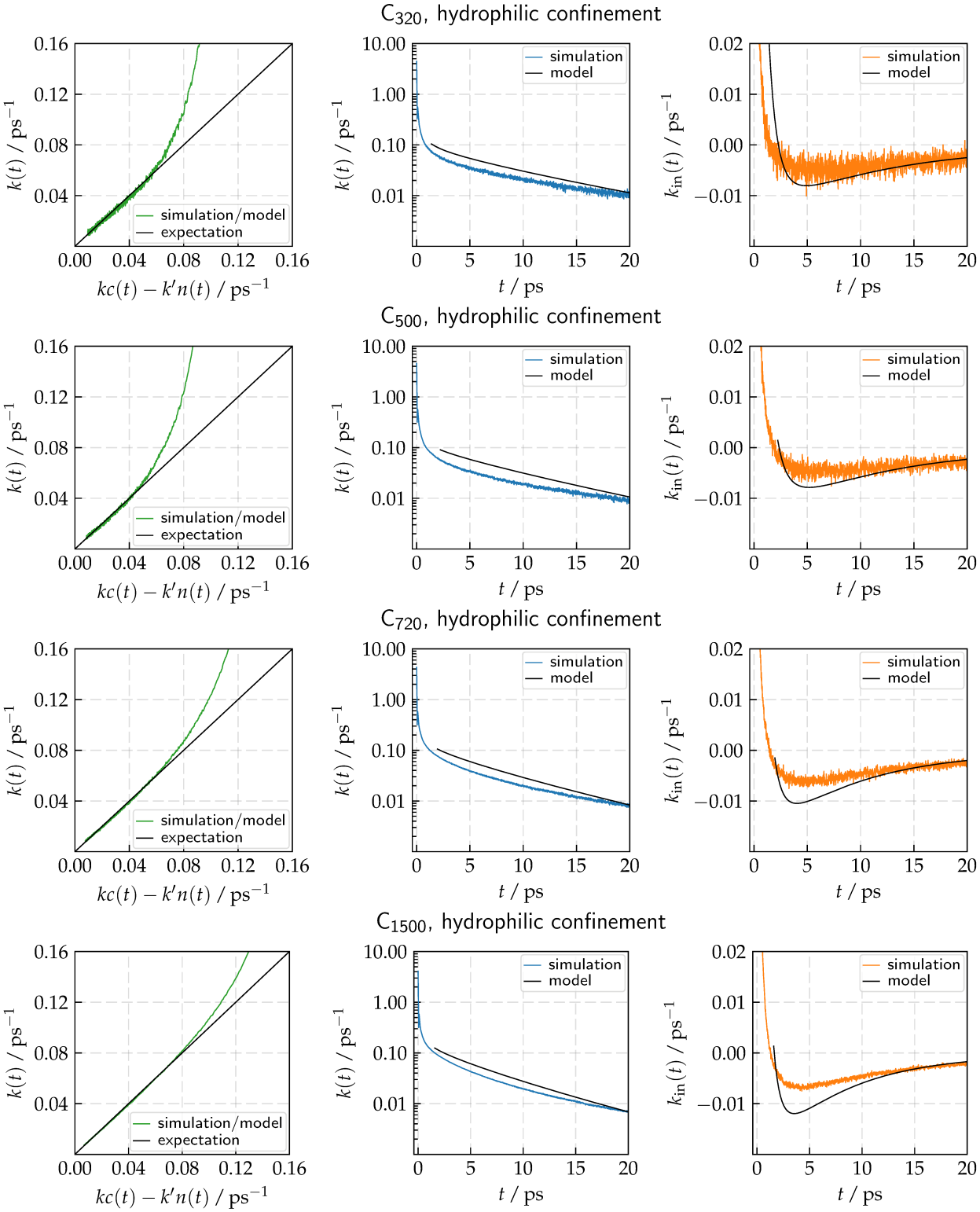

Figure S10: Correlation between the hydrogen bond kinetics phenomenology and simulation data, as well as the reactive flux time correlation functions $k(t)$ and $k_{\mathrm{in}}(t)$ and their respective model predictions (Equation (6); main text) in all hydrophilic confinements.

Table S1: Forward and backward rate constants k and k' (in units of ps^{-1}), describing the hydrogen bond kinetics, as well as diffusive time scales τ_d and hydrogen bond lifetimes $\tau_\mathrm{hb} = 1/k$ (in units of ps). Note that both k and k' can be varied by $\approx 10\,\%$, while still leading to acceptable model fits. Bulk values are $k = 0.35\,\mathrm{ps}^{-1}$, $k' = 0.72\,\mathrm{ps}^{-1}$, $\tau_\mathrm{d} = 0.46\,\mathrm{ps}$, and $\tau_\mathrm{hb} = 2.90\,\mathrm{ps}^{-1}$.

	hydrophilic				hydrophobic			
	k	k'	τ_d	τ_hb	k	k'	τ_d	τ_hb
C_{320}	0.21	0.54	0.77	4.76	0.30	0.89	0.56	3.33
C_{500}	0.19	0.40	0.66	5.26	0.33	0.82	0.52	3.08
C_{720}	0.26	0.57	0.59	3.92	0.33	0.76	0.52	3.08
C_{1500}	0.29	0.65	0.52	3.45	0.33	0.75	0.48	3.03

References

(1) Soper, A. K.; Castner, E. W.; Luzar, A. Impact of Urea on Water Structure: A Clue to its Properties as a Denaturant? *Biophys. Chem.* **2003**, *105*, 649–666.

(2) Chau, P.-L.; Hardwick, A. J. A New Order Parameter for Tetrahedral Configurations. *Mol. Phys.* **1998**, *93*, 511–518.

(3) Luzar, A.; Chandler, D. Hydrogen-Bond Kinetics in Liquid Water. *Nature* **1996**, *379*, 55–57.

(4) Luzar, A. Resolving the Hydrogen Bond Dynamics Conundrum. *J. Chem. Phys.* **2000**, *113*, 10663.

(5) Weiß, R. G.; Heyden, M.; Dzubiella, J. Curvature Dependence of Hydrophobic Hydration Dynamics. *Phys. Rev. Lett.* **2015**, *114*, 19–21.

ments, however, interfacial hydrogen bond dynamics has been observed to accelerate.[13] These results can be transferred to the air/water interface,[14,15] which may be considered as a special case of hydrophobic interfaces.

Drastically different results were observed in hydrophilic confinements, notably inside silica[16] and graphene oxide[17] nanopores, polyoxometalate nanocages,[18–21], at model interfaces,[12] and inside reverse micelles.[22–29] The latter two encapsulate nanoscopic pools of water inside well-characterized geometries and are particularly popular system choices in experimental studies. Through numerous computational[12,16,28,29] and experimental[22–27] studies, the unanimous picture of hindered translational motions across the interface, decelerated reorientation dynamics, and prolonged hydrogen bond lifetime has been established. These effects have often been attributed to the presence of hydrogen bonds between water and the interface. Furthermore, a core/shell model has been found to accurately describe many dynamic properties,[22–24] wherein the confined water molecules are divided into interfacial and bulk-like subensembles.[1] Inside polyoxometalate cages, a broad distribution of single particle relaxation times observed from quasi-elastic neutron scattering was suggested to originate from distinct local diffusivities.[18]

We performed molecular dynamics (MD) simulations of water inside nanoscopic model fullerenes (see Figure 1 for an example). These systems possess well-defined, almost spherical structures and can (with only minor modifications) be used to model the polyoxometalate cages investigated by other groups.[18–21] We chose a set of system sizes (C_{320} to C_{1500}) and two confinement–water interaction sets (a hydrophobic and a hydrophilic set) to shed light on the impact of the chemical nature of the confinement.

The study focuses on the calculation of diffusion tensors inside spherical nanocages, as prototypical nanoreactors. While various techniques exist to treat diffusion close to planar interfaces[10,30] or across membranes,[30] spherical symmetry has not been investigated before to the best of our knowledge. Since diffusion in bulk water is intimately connected to hydrogen bond kinetics,[31,32] we complement this article by a detailed discussion of this kinetics in spherical nanoconfinements.

[1]Note that in these models, effects of the core ensemble diminish in nanoscopic micelles ($\lesssim 1\,\mathrm{nm}$), where most water molecules are interfacial, and effects of the shell ensemble diminish in mesoscopic cavities ($\gtrsim 10\,\mathrm{nm}$), where most molecules are bulk-like.[22]

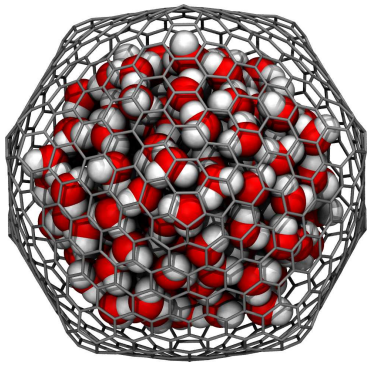

Figure 1: Snapshot of a C_{720} nanocage, filled with 145 water molecules.

Methods

Systems Investigated and Models

The model systems employed in this study consist of SPC/E[33] water molecules confined inside rigid structures that share their topology with the icosahedral fullerenes C_{320}, C_{500}, C_{720}, and C_{1500}. The use of this force field is motivated by our previous dynamic studies of confined water.[34–38] Other force field choices are available and equally valid. Our recent work showed considerable differences between mobilities of confined ions in nonpolarizable (SPC/E) and polarizable (SWM4-NDP/AH)[39] models, but comparatively small effects of the force field on the mobilities of water molecules.[38] The latter observation has been corroborated by a comparison of mobilities of SPC/E water with polarizable SWM4-NDP[39] or BK3 water[40] under external field.[41] In the present work, the emphasis is on the methodology for the calculation of local diffusivities, independently of the use of a specific potential. While tests with different force fields may show quantitative differences, we do not expect them to alter any of the con-

clusions of our study.

The confinement structures were generated by the program Fullerene with default parameters for all settings.[42] An overview of selected geometrical parameters and water occupation numbers is given in Table 1.

Distinctions were made between two water–confinement interaction parameter sets: an attractive one that is called hydrophilic and a less attractive one termed hydrophobic. The parameter sets are summarized in Table 2. Note that the hydrophilic confinements derive their hydrophilicity directly from enhanced Lennard-Jones interactions rather than by varied partial charges[44] on the confinement wall.

Grand Canonical Monte Carlo Simulations

In order to obtain the occupation numbers reported in Table 1, initially filled nanocages were held in apparent equilibrium with a bulk water surrounding by means of GCMC simulations. In these simulations, particle number fluctuations at constant volume V, temperature T, and chemical potential μ are accounted for by trial insertions and deletions of molecules in such a way that the grand canonical probability density is sampled.[45] The method thus mimics the experimental setup of an adsorption experiment. The chemical potential of water was chosen to obtain ambient pressure ($P = 0$ to 10 atm at $T = 298\,\mathrm{K}$) in separate bulk phase simulations. Monte Carlo simulations were performed using an in-house code. Methodological and algorithmic details have been described elsewhere.[46,47]

Molecular Dynamics Simulations

MD simulations were performed in the microcanonical (NVE) ensemble, which permits a highly accurate description of dynamics, without bias by thermostats or barostats. This comes at the cost of sacrificing the convenience of setting up the simulation at a specified temperature, which allows easy comparisons between simulations of differently sized nanocages and with experiments. To circumvent this problem, care was taken in setting up the initial velocities so that the average temperature after equilibration was within the range of $(300 \pm 3)\,\mathrm{K}$ and that the total angular momentum of the system was zero. Since the angular momentum is a conserved quantity in non-periodic NVE simulations, it remains zero if the time integration is accurate enough. The equations of motion were solved by Velocity-Verlet integration with a time step of 2 fs. Initial configurations were taken from the Monte Carlo simulations. Water molecules were kept rigid by the SHAKE algorithm. Fullerene atoms were not propagated, remaining at fixed positions. All quantities except for diffusion were calculated from 5 ns trajectories with snapshots written to file every second time step. Transition counts between radial and angular bins needed for the calculation of diffusion constants were collected over 100 ns with snapshots written every 500th time step. In these long simulations, an energy drift in the NVE ensemble is unavoidable (see Table 3). The chosen time step is a compromise between accurate time integration needed to keep the energy drift small and computational efficiency. Furthermore, the energy drift was minimized by refraining from cutting off Lennard-Jones interactions and from using long-range electrostatic solvers, such as the Ewald sum. Instead, the full Coulomb sum was calculated, consistent with the lack of periodicity in our finite-sized systems. All MD simulations were performed using the Lammps molecular dynamics software.[48]

Diffusion

Spherical nanocages break the homogeneity and isotropy of the confined liquid, rendering conventional approaches to diffusion coefficients useless (i.e., fitting the mean-squared displacement as a function of time). Instead of a single diffusion coefficient D_0 that describes the motions of water molecules within the averaged potential exerted by their surroundings, an anisotropic and position dependent diffusion tensor $\mathbf{D}(\mathbf{r})$ must be employed. Spherical symmetry implies that diffusion in radial direction (orthogonal to the interface, denoted by $\perp$) differs from diffusion in angular direction (parallel to the interface, denoted by $\parallel$) and both depend on the radial

Table 1: Maximum inner sphere radius r_{mis} and cage volume V_{cage} of the fullerenes, as well as water occupation numbers N_{water} and their standard deviations σ_N in differently parameterized (hydrophilic and hydrophobic) systems. Geometrical parameters were calculated by the program Fullerene.[42]

Fullerene	r_{mis}/nm	V_{cage}/nm^3	$N_{\mathrm{water}}^{\mathrm{hydrophilic}}$	$N_{\mathrm{water}}^{\mathrm{hydrophobic}}$	σ_N
C_{320}	0.762	2.02	31	25	1
C_{500}	0.954	3.97	79	65	1
C_{720}	1.146	6.87	145	130	2
C_{1500}	1.641	20.73	501	473	3

Table 2: Lennard-Jones parameters σ_{CO} and ϵ_{CO} and the corresponding microscopic contact angles θ_{m} on a planar graphite-like surface, reported in ref.[43].

	σ_{CO}/nm	ϵ_{CO}/kJ mol^{-1}	θ_{m}/deg
hydrophilic	0.319	0.6270	29.4
hydrophobic	0.319	0.3762	101.2

Table 3: Average temperature $\langle T \rangle$ of the 100 ns trajectories, the corresponding standard deviations σ_T, and the energy drift ΔT, calculated from the difference between initial and final temperatures, which were determined by linear regression of the temperature time series.

		$\langle T \rangle$ /K	σ_T/K	ΔT/K
hydrophilic	C_{320}	297.9	25.0	−3.1
	C_{500}	298.6	15.9	−3.7
	C_{720}	298.1	11.7	−3.5
	C_{1500}	297.7	6.4	−3.5
hydrophobic	C_{320}	300.6	28.4	−3.3
	C_{500}	300.7	17.8	−3.5
	C_{720}	298.5	12.3	−3.2
	C_{1500}	297.6	6.6	−3.6

position within the nanocage.

The prediction of such diffusion tensors is conceptually challenging, since it requires the solution of the full Smoluchowski equation,

$$\frac{\partial p\left(\mathbf{r},t\right)}{\partial t} = \boldsymbol{\nabla} \cdot \left[\mathbf{D}\left(\mathbf{r}\right) e^{-\beta F(\mathbf{r})} \boldsymbol{\nabla} \left(e^{\beta F(\mathbf{r})} p\left(\mathbf{r},t\right) \right) \right] , \tag{1}$$

where $p\left(\mathbf{r},t\right)$ is the spatial probability density of a tracer particle as a function of time, $\beta = 1/kT$, and $F\left(\mathbf{r}\right)$ is the position dependent free energy (potential of mean force). Fortunately, the problem is formally equivalent to pair diffusion, which has received significant theoretical attention.[49]

Here, we adopt the original approach of Hummer[49,50] to self-consistently estimate local diffusion coefficients and free energies from simulation data. The method relies on separation of the Smoluchowski equation into a set of uncoupled, one-dimensional differential equations and subsequent solution by spatial discretization and inference of model parameters from simulation data through Bayesian inference.[50,51]. The approach is also applicable to the diffusion of guest solute molecules[52] in the present geometry.

The diffusion tensor $\mathbf{D}\left(\mathbf{r}\right)$ shows spherical symmetry in the investigated nanocages, that is,

$$\mathbf{D}\left(\mathbf{r}\right) = \begin{pmatrix} D_{\perp}\left(r\right) & 0 & 0 \\ 0 & D_{\parallel}\left(r\right) & 0 \\ 0 & 0 & D_{\parallel}\left(r\right) \end{pmatrix} , \tag{2}$$

in spherical coordinates r, θ, ϕ. The Smoluchowski equation (Equation 1) in such a coordinate system can be solved by means of Green's functions $P\left(r, \cos\theta, t | r', 0\right) = r^2 p\left(r, \theta, t | r', 0, 0\right)$,

which measure the conditional probability of finding a tracer particle in the intervals $(r, r+dr)$ and $(\cos\theta, \cos\theta + d\cos\theta)$ starting from r' and $\theta = 0$ at time 0. As demonstrated by Mittal and Hummer,[49] the diffusion equation for these functions becomes

$$\frac{\partial}{\partial t}P = \frac{\partial}{\partial r}\left\{D_\perp(r)\left[\beta V'(r) + \frac{\partial}{\partial r}\right]P\right\} + \frac{D_\parallel(r)}{r^2}\frac{\partial}{\partial \cos\theta}\left[\left(1-\cos^2\theta\right)\frac{\partial}{\partial \cos\theta}P\right], \quad (3)$$

where $V(r) = F(r) - 2kT\ln r$ and $V' = dV(r)/dr$. It can be further reduced by integration over the angular part, leading to

$$\frac{\partial}{\partial t}G = \frac{\partial}{\partial r}\left[D_\perp(r)\left(\beta V'(r) + \frac{\partial}{\partial r}G\right)\right], \quad (4)$$

wherein the radial propagator $G(r, t|r', 0) = \int_{-1}^{1} P(r, \cos\theta, t|r', 0)\, d\cos\theta$ measures the conditional probability of finding a tracer particle in the interval $(r, r+dr)$ at time t, starting from r' at time 0, irrespective of angular motion. The preceding equation permits the treatment of radial diffusion as a standard one-dimensional problem. After realizing that the bottom term in Equation 3 corresponds to the angular momentum operator in quantum mechanics, angular diffusion can be treated by a set of uncoupled one-dimensional equations, which are obtained after expanding the Green's function $P(r, \cos\theta, t|r', 0)$ in Legendre polynomials $p_l(x)$:

$$P(r, \cos\theta, t|r', 0) = \sum_{l=0}^{\infty}\frac{2l+1}{2}p_l(\cos\theta)\, Q_l(r, t|r', 0). \quad (5)$$

The associated evolution equations for each of the Q_l are given by:

$$\frac{\partial}{\partial t}Q_l = \frac{\partial}{\partial r}\left\{D_\perp(r)\left[\beta V'(r) + \frac{\partial}{\partial r}Q_l\right]\right\} - \frac{D_\parallel}{r^2}l(l+1)\, Q_l, \quad (6)$$

which are equal to Equation 4 for $l = 0$ and differ therefrom by sink terms for $l > 0$. Note that for practical reasons, Equation 5 has to be truncated after a finite number of terms in computer codes. In this work, the sum was terminated at $l_{\max} = 30$. No significant changes in results could be observed by taking terms of higher order into account.

In the following, the algorithm to calculate radial diffusion coefficients $D_\perp(r)$ shall be outlined. To do so, simulation trajectories were discretized by assigning radial positions r into corresponding bins i along r, and then counting the number of events N_{ji} when a particular water molecule was in bin i at some time t during the simulation and in bin j at time $t + \Delta t$ later. In this work, bins of equal radial width $\Delta r = 0.05\,\text{nm}$ were chosen. Within the long (100 ns) equilibrium trajectories, transition counts are symmetric (i.e., $N_{ij} = N_{ji}$), as demanded by microscopic time reversibility. Care must be taken in choosing the lag time Δt, so that the influence of the free energy surface underlying the particle dynamics has already been felt. In the present simulations, lag times of 1 ps, 2 ps, 5 ps and 10 ps were used. After counting the transitions, radial diffusion coefficients $D_\perp(r_i)$ and free energies $F(r_i)$[2] that are consistent with the observed data were estimated by a Bayesian inference approach.[50,51] In the Bayesian formalism, a posterior distribution $p(\text{parameters}|\text{data})$ of the model parameters is constructed from the simulation data through the Bayes theorem

$$p(\text{parameters}|\text{data}) \propto p(\text{data}|\text{parameters})\, p(\text{parameters}), \quad (7)$$

wherein $p(\text{parameters})$ is the prior distribution of parameters, which is assumed to be uniform, and $p(\text{data}|\text{parameters})$ is given by a likelihood function, which is a product of Green's functions expressed in terms of matrix exponentials.[50] To construct posterior distributions, parameters were sampled using Metropolis Monte Carlo simulations in parameter space. For technical details, the reader is referred to ref.[51].

Once $D_\perp(r)$ and $F(r)$ have been determined,

[2] Evaluated at the position r_i of the bin center for $D_\perp$ and at the position of the bin edges for V.

angular diffusion coefficients $D_{\parallel}(r)$ can be estimated in a similar fashion. Here, the numbers $N_{j\alpha,i}$ for transitions of a particle from radial bin i to radial bin j and angular bin α have to be counted. Angular bins were indexed according to the cosine of the azimuthal angle

$$\cos\theta(t) = \frac{\mathbf{r}(t)\cdot\mathbf{r}(0)}{r(t)\,r(0)}\,, \tag{8}$$

with $\theta(0) = 0$ by definition of the coordinate system and without loss of generality. Here, the azimuthal angle was divided into 50 bins of equal width. A second Bayesian inference approach can be devised as outlined above to find the set of angular diffusion coefficients $D_{\parallel}(r_i)$ that is most consistent with the observed simulation data.

To enforce a certain degree of smoothness on the resulting free energy and diffusion profiles, they were treated internally as a set of continuous cubic splines, with the number of spline nodes set to the number of distinct features (maxima + minima) seen in the radial density profiles. Finally, a procedure similar to shifting the origin of time in free diffusion (i.e., fitting the mean-square displacement to $6D_0(t+\tau)$, with τ being the origin of time) was employed to account for the initial non-diffusive spread of molecules due to fast molecular motions. Therefore, transition counts were collected at several different lag times and the origin of time was optimized during the MC parameter sampling, as well.

Hydrogen Bond Kinetics

We invoked the Luzar/Chandler model[31,32] (originally developed for bulk water) to describe hydrogen bond kinetics inside our model cavities by a set of well-defined rate constants k and k', associated with hydrogen bond breaking and reforming, respectively. Since most molecules are interfacial in our confinements and since there is only one type of hydrogen bonds present in these systems (water–water hydrogen bonds), assuming a single set of rate constants should be a reasonable approximation.

We measure the decay of hydrogen bond populations in terms of the hydrogen bond time-correlation function

$$c(t) = \frac{\langle \delta h(t)\,\delta h(0)\rangle}{\left\langle [\delta h(0)]^2\right\rangle}\,, \tag{9}$$

and its reactive flux $k(t) = -\,dc/dt$. Therein, the binary, dynamical hydrogen bond operator $h(t)$ equals one if a hydrogen bond exists between a tagged pair of water molecules (and zero otherwise), and the term $\delta h(t)$ measures fluctuations of $h(t)$ around its equilibrium average.

The employed model assumes a reversible chemical reaction between hydrogen bonded pairs of water molecules (measured in terms of $c(t)$) and those pairs that are not hydrogen bonded, but have not diffused apart (measured in terms of $n(t)$)

$$c(t) \underset{k'}{\overset{k}{\rightleftharpoons}} n(t)\,. \tag{10}$$

The latter time-correlation function is defined through

$$n(t) = \frac{\langle H(t)\,[1-\delta h(t)]\,\delta h(0)\rangle}{\left\langle [\delta h(0)]^2\right\rangle}\,, \tag{11}$$

and its reactive flux is $k_{\mathrm{in}}(t) = -\,dn/dt$. The binary dynamical variable $H(t)$ equals one if both tagged water molecules are within their first solvation shell. For the model to be true, the following phenomenological relation must hold for times t larger than a transient period t_{trans}, wherein the decay of hydrogen bond populations is primarily driven by librations and interoxygen vibrations:

$$-\frac{d\,c(t)}{dt} = k(t) = kc(t) - k'n(t)\,. \tag{12}$$

The pair of rate constants (k, k') is found by minimizing deviations between both sides of the equation.

The following geometric criteria were used to define the binary operators h and H:

$$h = \theta(R_c - R)\,\theta(r_c - r)\,\theta(\phi_c - \phi)\,, \tag{13}$$

$$H = \theta(R_c - R)\,. \tag{14}$$

Therein, R denotes the O$\cdots$O separation of

the tagged pair, r is the O···H intermolecular separation, ϕ is the angle between the O···O vector and the covalent OH-bond, and the index c denotes the respective cutoff value. $\theta(x)$ is the Heaviside step function. The required cutoff values were set to $R_c = 0.35\,\mathrm{nm}$, $r_c = 0.245\,\mathrm{nm}$, and $\phi_c = 30°$.[31,32]

Results and Discussion

Occupation Numbers

Realistic occupation numbers N_{water} (Table 1) corresponding to the ambient chemical potential of water were calculated from grand canonical Monte Carlo (GCMC) simulations in order to make meaningful comparisons with experimental setups. The resulting average particle number densities $\tilde{\rho}$ are visualized in Figure 2. Note that our occupation numbers differ significantly from numbers obtained by others,[53] using an extrapolation scheme based on occupation numbers from ab initio studies in smaller nanocages. Because of the layered structure of confined water shown in the following section, densities do not increase linearly and similar effects manifest themselves throughout all quantities investigated in this article.

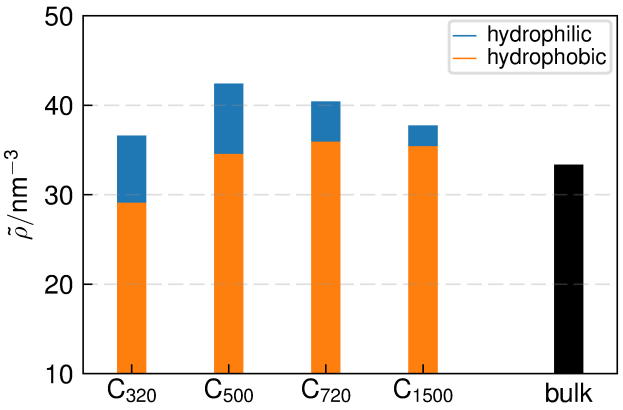

Figure 2: Average particle number density $\tilde{\rho} = N_{\mathrm{water}}/V_{\mathrm{cage}}$ in the hydrophilic and hydrophobic confinements, as well as in a bulk water system at ambient conditions. V_{cage} is the solvent accessible nanocage volume, determined by Monte Carlo integration of the region where the carbon–oxygen Lennard-Jones potential $v_{\mathrm{LJ}}(r) < kT$. Note that the apparent densities are very sensitive to this normalizing volume.

Radial Structure

Packing effects, geometrical restrictions, and specific interactions lead to a non-uniform potential of mean force within the nanocages associated with a layer structure (Figure 3). These radial density profiles show many analogies to planar interfaces.[54] However, some peculiarities arise due to the near-spherical nature of the nanocages. Overall, local densities are consistently higher in the hydrophilic confinements, in which the enhanced attractiveness of the nanocage and the elevated occupation numbers induce a much more structured water droplet. Within the core regions of the nanocages, the layering levels off and the bulk density ($33.4\,\mathrm{nm}^{-3}$) is approached with increasing nanocage size. Note that fullerenes are slightly aspherical and density profiles do not drop abruptly to zero at the confinement boundaries. At large radii, they show a small shoulder in the density profiles.

While the local water density fluctuates quite remarkably, even in the center of the nanocages, the hydrogen bond network is hardly disturbed beyond the interfacial region, as demonstrated by tetrahedral order parameters and hydrogen bond number profiles (Figures S1–S3; Supporting information).

From a structural point of view, all investigated properties support the concept of a core/shell model,[22–24] wherein water molecules are divided into subensembles that are bulk-like and interfacial. However, the bulk-like phase occupies only a minor fraction of the total system volume inside our small nanocages, so that most water molecules can be considered to be interfacial. In our grand-canonically filled nanocages, we do not observe the formation of cage-like[53] water structures.

Diffusion

From an atomistic point of view, (self-)diffusion can be considered as the result of a random walk of a single particle in the mean field of all others. It describes the complex many-particle dynamics

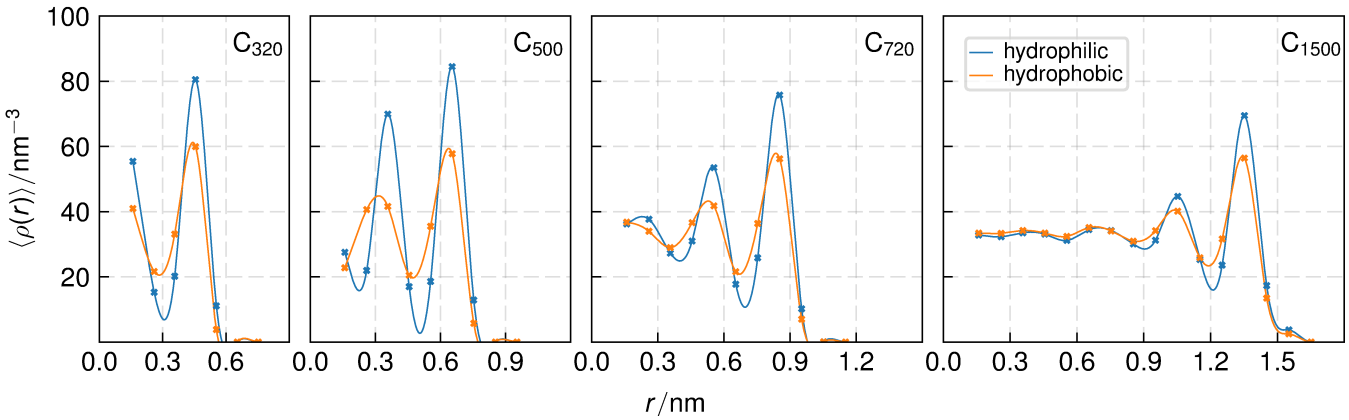

Figure 3: Local average particle number density $\langle \rho(r) \rangle$ as a function of the radial distance r from the nanocage center. Lines are meant to guide the eye.

as an average, single-particle motion. A priori, there is no reason to believe that a diffusive picture should hold in spherical nanoconfinement, but we shall demonstrate its validity in the following.

Position dependent radial and angular diffusion constants, as well as free energies have been calculated in both hydrophilic and hydrophobic confinements (Figures 4 and 5) and the following observations can be made:

1. Radial diffusion coefficients $D_{\perp}(r)$ are correlated with free energy profiles, that is, particles residing at energetically favorable positions are less likely to move away in radial direction and vice versa.

2. Angular diffusion coefficients $D_{\parallel}(r)$ are anti-correlated with free energy profiles, that is, angular motion is enhanced at positions of increased density.

3. With increasing nanocage size, both diffusion tensor components converge to a limiting value of about $2\,\mathrm{nm^2\,ns^{-1}}$ as $r \to 0$. Because of the known system size dependence[55] of diffusion coefficients, the limiting value is expected to be smaller than the corrected bulk value[56] of SPC/E water ($D_0 = 2.97\,\mathrm{nm^2\,ns^{-1}}$).

4. Overall, diffusion coefficients are larger in the hydrophobic confinements. These effects are particularly pronounced for the angular diffusion coefficients, which are considerably elevated close to hydrophobic interfaces.

The radial diffusivity profiles in our largest cavities compare well with similar studies at planar hydrophilic and hydrophobic interfaces, except that the interfacial diffusivity drop in our hydrophilic model systems is much less pronounced than in the corresponding planar interfaces that exhibit explicit hydrogen bonds.[12] The lack of such hydrogen bonds also explains the increase in the interfacial perpendicular diffusivity, which others[12,16] have observed to decrease. Consistent with these considerations, we see no difference in the phase modulation of the diffusivity oscillations between hydrophilic and hydrophobic cavities, which could be attributed to a different mechanism of local water dynamics in the presence/absence of interfacial hydrogen bonds.[12]

We observe non-monotonicities in the interfacial diffusivities with respect to the cavity size (Fig. S7), reminiscent of those observed at convex hydrophobic interfaces.[57] Despite this similarity, the underlying mechanisms cannot be the same, since concave nanocages do not support a structural crossover analogous to that observed in the hydration shell of convex solutes.

Note that the free energy profiles, which are a direct result of the Bayesian sampling procedure, are also accessible from conventional counting statistics $F(r) = -kT \ln p(r)$, where $p(r)$ is the probability density of finding a particle at position r. Both are in perfect agreement (Figure S4).

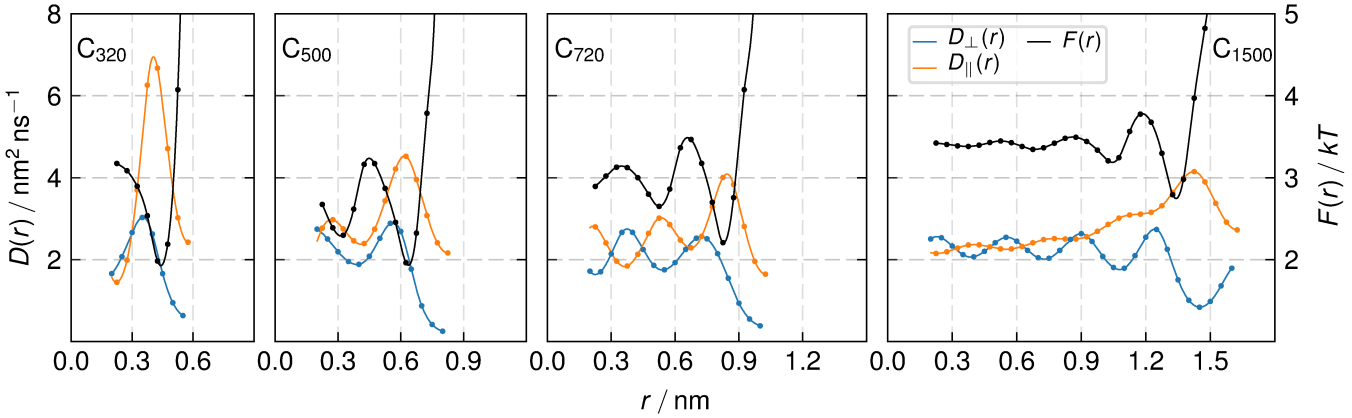

Figure 4: Position dependent diffusion constants $D_\perp(r)$ and $D_\parallel(r)$, as well as free energy profiles $F(r)$ as a function of the distance r from the nanocage center in the hydrophobic confinements. Lines show the model-intrinsic spline representation of the discrete data.

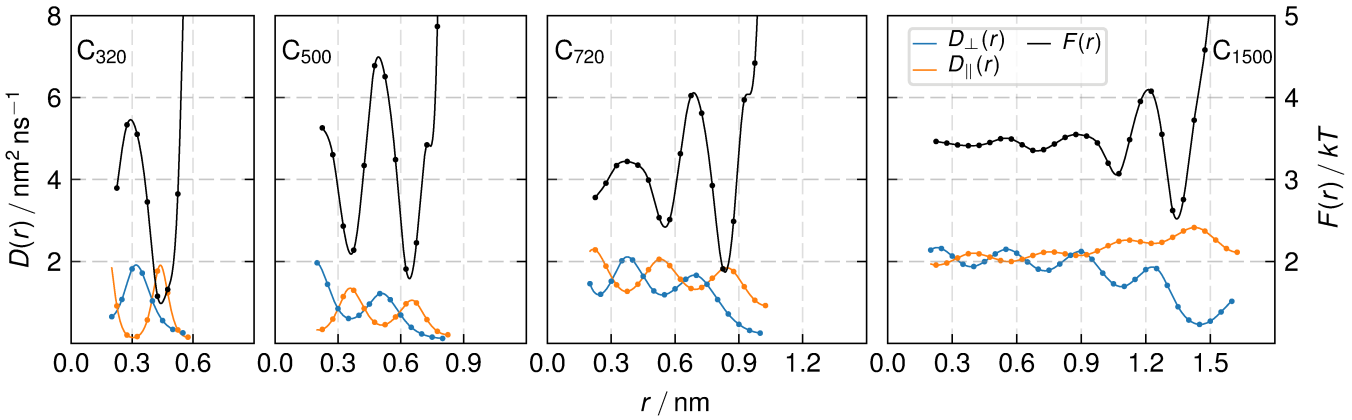

Figure 5: Position dependent diffusion constants $D_\perp(r)$ and $D_\parallel(r)$, as well as free energy profiles $F(r)$ as a function of the distance r from the nanocage center in the hydrophilic confinements. Lines show the model-intrinsic spline representation of the discrete data.

In order to judge the quality of the proposed diffusion model, we compare propagators $G(r,t|r',0)$ and $P(r,t,\cos\theta|r',0)$ (in radial and angular direction, respectively) to the actual transition probabilities observed during our MD simulations. These functions measure the conditional probability of finding a particle that was initially at radial position r' at a new position r, after a lag time t has passed. In angular direction, the particle simultaneously performs an angular motion of θ degrees. Visualizing the complete set of propagators is cumbersome—however, general trends can be demonstrated with the aid of the selected examples presented in the following. Further data (in particular all results for the hydrophilic confinements) can be found in the Supplementary Information.

Radial propagators $G(r,t|r',0)$ are shown in Figure 6 for the hydrophobic confinements. Therein, the color gradient indicates increasing values of r', with purple lines corresponding to an initial position r' at the center of the nanocage and yellow lines corresponding to the outermost positions. The agreement between the propagators predicted by our diffusion model and the actual simulation results is remarkable, proving the model's quantitative validity.

Angular propagators $P(r,\cos\theta,t|r',0)$ are shown in Figure 7 for the hydrophobic confinements. Here, we only show propagators for particle motions originating from the important interfacial density layer (i.e., propagators have been evaluated the location of the interfacial density maximum $r' = r_{\max}$). The color gradient in Figure 7 indicates decreasing values of $\cos\theta$, with purple lines corresponding to $\theta = 0$ and yellow lines corresponding to the value indicated in the different panels. Larger angular jumps than those shown in Figure 7 are very unlikely, as demonstrated by the $\cos\theta$ dependence of the angular propagators. Thus the shown set of propagators covers the most likely angular motions of water molecules inside our nanocages. In angular direction, agreement between model and simulation data is less precise, but still quantitatively convincing. Discrepancies arise mostly for low-probability motions.

In conclusion, both radial and angular propagators demonstrate that diffusion is highly inhomogeneous within spherical nanocages and that the predicted diffusion coefficients (Figures 4, 5) are quantitatively accurate.

Hydrogen Bond Kinetics

Diffusion and hydrogen bond kinetics are intimately connected.[31,32] A hydrogen bond can only break permanently if the bonding partners have diffused apart. In bulk water, this coupling of dynamical processes operating on similar timescales causes a non-exponential decay of hydrogen bond populations, measured in terms of the hydrogen bond time-correlation function $c(t)$ and its reactive flux $k(t)$. We observe a qualitatively similar, non-exponential decay in our nanocages (Figures 8, S9, S10).

We prove the validity of the phenomenological description (Equation 10) in Figure 9, left panel, (as well as in Figures S9, S10), which show direct correlations between model and simulation data for transient times larger than $\sim 1.5\,\mathrm{ps}$. The corresponding rate constants k and k' are listed in Table S1 and visualized in Figure 10. In all investigated nanocages, the rate constants of hydrogen bond breaking k (or inverse hydrogen bond lifetimes $\tau_{\mathrm{hb}} = 1/k$) are smaller than in the bulk phase. Similar to the behavior of the densities, the slow-down is non-monotonic, because of the layered structure of water. Furthermore, all effects are more pronounced in hydrophilic confinement. These findings are in contrast, to a similar study, where accelerated hydrogen bond dynamics has observed.[53] The differences can most likely be attributed to the neglect of diffusion-correction, as well as to the different occupation numbers used in ref. 53.

Luzar and Chandler argued that if diffusion is indeed the cause of the non-exponential decay of $c(t)$, then it should be possible to reconstruct the flux of both independent time- correlation functions, $k(t) = -dc/dt$ and $k_{\mathrm{in}}(t) = -dn/dt$, from solutions of a coupled diffusion kinetic equation.[31,32] On time scales that are longer than the transient regime and on length scales that are larger than the spatial extent of a hydrogen bond, the following modified Fick's law for pair

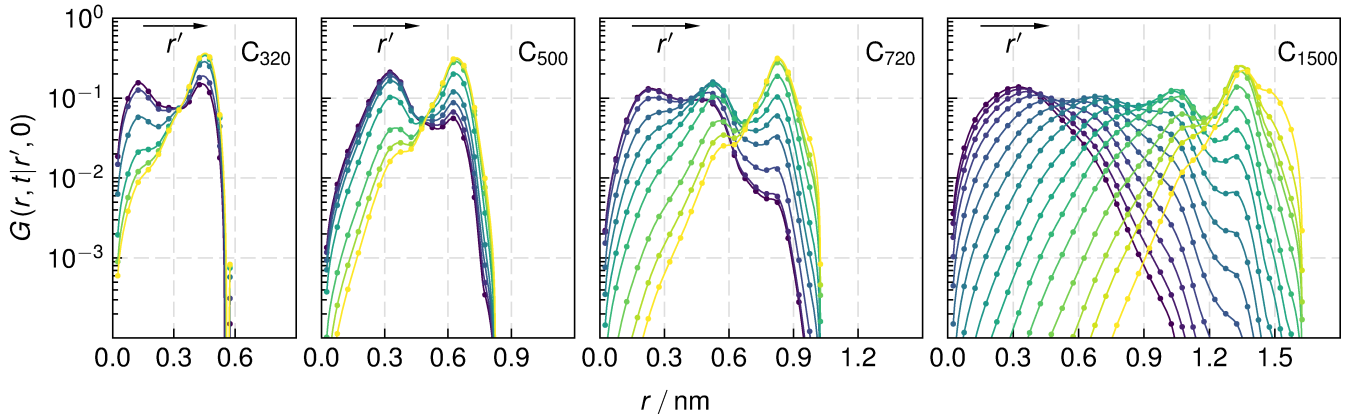

Figure 6: Model propagators $G\,(r, t|r', 0)$ (solid lines) compared to simulation data (symbols) in the hydrophobic confinements for a lag time of 10 ps. The color gradient indicates increasing initial positions r'.

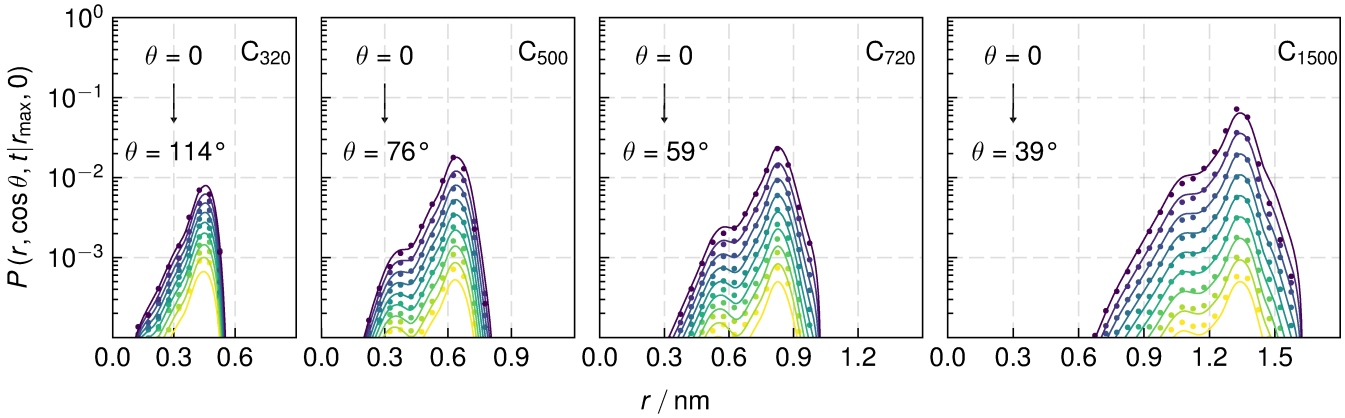

Figure 7: Model propagators $P\,(r, \cos\theta, t|r', 0)$ (solid lines) compared to simulation data (symbols) in the hydrophobic confinements for a lag time of 10 ps. The initial position of the particle has been restricted to the interfacial density maximum $r' = r_{\max}$ in this plot. The color gradient indicates decreasing values of $\cos\theta$.

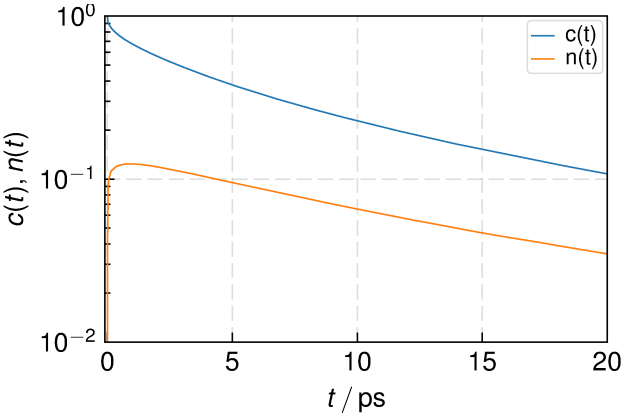

Figure 8: Hydrogen bond time-correlation functions $c(t)$ and $n(t)$ inside C_{500}, hydrophobic. The time evolution of $c(t)$ and $n(t)$ in the other confinements is qualitatively similar and results are shown in the Supplementary Information.

diffusion should hold:

$$\frac{\partial p\left(\mathbf{r},t\right)}{\partial t} = D\boldsymbol{\nabla}^2 p\left(\mathbf{r},t\right) + \delta\left(\mathbf{r}\right)\left[kc\left(t\right) - k'n\left(t\right)\right] , \tag{15}$$

Therein, $p\left(\mathbf{r},t\right)$ is the time and distance dependent density of the diffusing unbonded pair, $\mathbf{r}$ is the vector between the pair, and $D = 2D_0$ is the pair diffusion coefficient of water. In this equation, pair diffusion is subject to source and sink terms corresponding to hydrogen bond breaking and reforming. Such effects are only relevant on length scales where a hydrogen bond may exist. The delta function $\delta\left(\mathbf{r}\right)$ localizes the source and sink terms to such length scales. Results of this equation depend on a free parameter τ_d that characterizes the time required for an unbound pair of water molecules to diffuse apart (escape time).[31,32] In combination with the hydrogen bond lifetime τ_hb, the escape time τ_d defines the mean residence time $\tau_\mathrm{res} = \tau_\mathrm{hb} + \tau_\mathrm{d}$ of a water molecule within the first coordination shell of a hydrogen bond partner.[58] Escape times are listed in Table S1 and visualized in Figure 10.

Note that the preceding formalism has been derived for bulk water, where diffusion is isotropic and homogeneous. Equation 15 cannot be expected to hold quantitatively inside our nanocages, as demonstrated by the anisotropic and strongly position-dependent diffusion profiles presented in the previous section. However, given that most molecules are interfacial in our nanocages and subject to an average diffusion coefficient $\tilde{D} = \frac{1}{3}\left[D_\perp(r_\mathrm{max}) + 2D_\parallel(r_\mathrm{max})\right]$, qualitative agreement between simulation and model can be achieved (Figures 9, S9, S10).

Correlations between the diffusion model presented in the previous section and the hydrogen bond kinetics phenomenology presented here can be illuminating. Consider the mean residence times τ_res of water molecules inside the coordination sphere of a hydrogen bond partner. If the system size dependence of these time scales is eliminated by considering the ratios $\tau_\mathrm{res}^\mathrm{philic}/\tau_\mathrm{res}^\mathrm{phobic}$ for a given nanocage size, correlation with average diffusion coefficients can be observed (Figure 11), proving that at room temperature, the strong coupling between diffusion and hydrogen bond kinetics, previously observed in bulk water,[31,32] also persists in spherical nanoconfinements.

Conclusion

We have presented a new method to calculate position-dependent diffusion coefficients in spherical nanocages based on Bayesian inference of model parameters from simulation data. The resulting diffusion profiles are anisotropic and strongly inhomogeneous, and the corresponding propagators show a remarkable agreement with direct transition probabilities (four orders of magnitude). Thus, our simulation results directly confirm previous interpretations of quasi-elastic neutron scattering data in terms of local diffusion models.[18] In terms of overall magnitude, diffusion coefficients are larger in hydrophobic confinement, especially in angular direction. Similar effects have also been observed close to planar interfaces.[10]

Despite such strong inhomogeneities in diffusion and local potentials of mean force, the tetrahedral hydrogen bond network in water is hardly disturbed beyond the interfacial water layer. Furthermore, a similar resilience can be seen in the dynamics of the hydrogen bond network. Hydrogen bond breaking and reforming can be quantitatively described by a single set of well-defined rate constants (or inverse lifetimes) if the effects of diffusion are eliminated. The

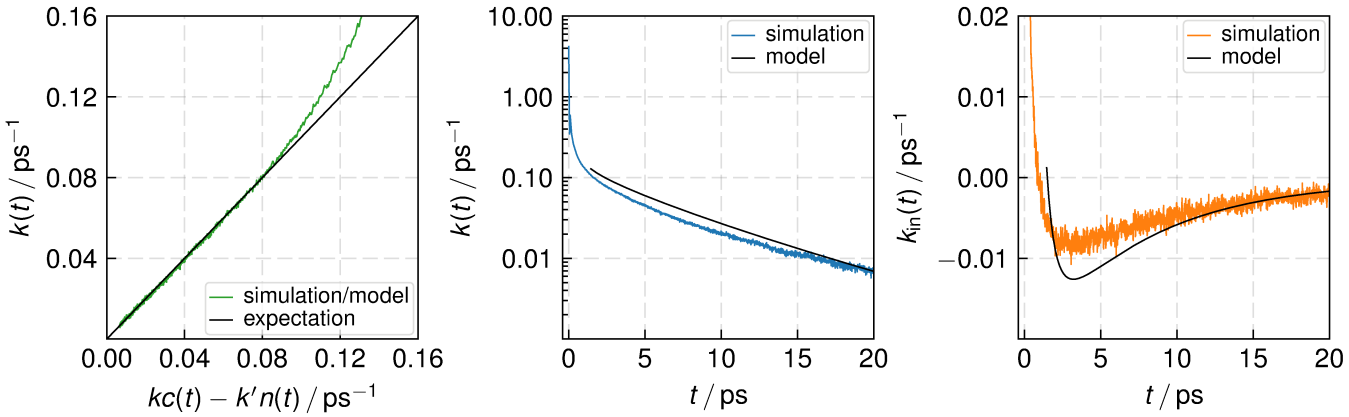

Figure 9: Correlation between the hydrogen bond kinetics phenomenology and simulation data, as well as the reactive flux time-correlation functions $k(t)$ and $k_{\mathrm{in}}(t)$ and their respective model predictions in C_{500}, hydrophobic. Results in the other confinements are qualitatively similar and are shown in the Supplementary Information.

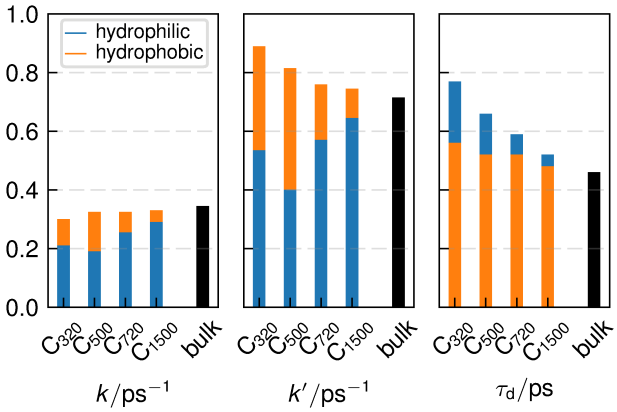

Figure 10: Rate constants of hydrogen bond breaking k and reforming k', as well as escape times τ_{d} in the confinements and in the bulk.

validity of the corresponding phenomenology in spherical confinement has been established by means of the correlation plots, which are straight lines on time scales where the model can be expected to hold. Our study demonstrates that correct treatment of diffusion in hydrogen bond kinetics leads to qualitatively and quantitatively different hydrogen bond lifetimes than those reported in a related study.[53] Finally, by invoking a simple model, hydrogen bond time-correlation functions have been reconstructed and agree with direct simulation data. The correlation between residence times and average diffusion coefficients is remarkable and demonstrates once more the intimate interconnection between diffusion and hydrogen bond dynamics.

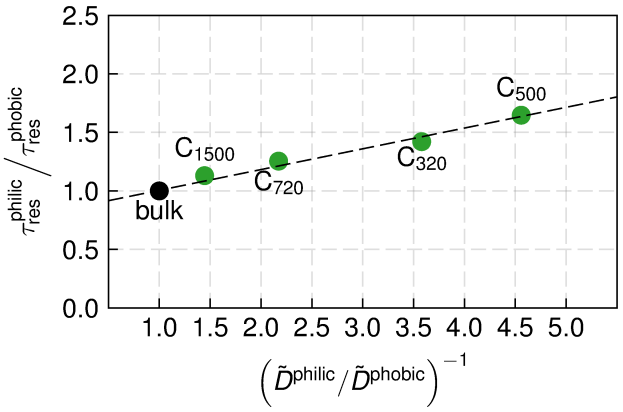

Figure 11: Correlation between residence times τ_{res} and average diffusion coefficients in the interfacial water layer $\tilde{D}$. Deviations from unity slope are a measure for the static differences in wettability between different nanocage parameterizations.

Acknowledgement This work was supported by the U.S. Department of Energy, Office of Basic Sciences (DE-SC 0004406) in the early stage, and by the National Science Foundation (CHE-1800120) in the late stage. G. H. thanks the Max Planck society for support. We also acknowledge supercomputing time allocations from the Extreme Science and Engineering Discovery Environment (XSEDE), supported by NSF Grant No. OCI-1053575, and the National Energy Research Scientific Computing Center (NERSC), supported by the Office of Science of the U.S. Department of Energy (DEAC02-05CH11231).

Supporting Information Available: Structural and dynamical data for all investigated systems and water–wall parameterizations not shown here. This material is available free of charge via the Internet at `http://pubs.acs.org/`.

References

(1) Petrosko, S. H.; Johnson, R.; White, H.; Mirkin, C. A. *J. Am. Chem. Soc.* **2016**, *138*, 7443–7445.

(2) Williams, D. E.; Dolgopolova, E. A.; Pellechia, P. J.; Palukoshka, A.; Wilson, T. J.; Tan, R.; Maier, J. M.; Greytak, A. B.; Smith, M. D.; Krause, J. A.; Shustova, N. B. *J. Am. Chem. Soc.* **2015**, *137*, 2223–2226.

(3) Grochmal, A.; Prout, L.; Makin-Taylor, R.; Prohens, R.; Tomas, S. *J. Am. Chem. Soc.* **2015**, *137*, 12269–12275.

(4) Roa, R.; Kim, W. K.; Kanduc, M.; Dzubiella, J.; Angioletti-Uberti, S. *ACS Catal.* **2017**, *7*, 5604–5611.

(5) Hummer, G.; Rasaiah, J. C.; Noworyta, J. P. *Nature* **2001**, *414*, 188.

(6) Hanasaki, I.; Nakatani, A. *J. Chem. Phys.* **2006**, *124*, 144708.

(7) Hummer, G. *Mol. Phys.* **2007**, *105*, 201–207.

(8) Rasaiah, J. C.; Garde, S.; Hummer, G. *Annu. Rev. Phys. Chem.* **2008**, *59*, 713–740.

(9) Striolo, A. *Nano Lett.* **2006**, *6*, 633–639.

(10) Liu, P.; Harder, E.; Berne, B. J. *J. Phys. Chem. B* **2004**, *108*, 6595–6602.

(11) Chowdhary, J.; Ladanyi, B. M. *J. Phys. Chem. B* **2008**, *112*, 6259–6273.

(12) Sedlmeier, F.; von Hansen, Y.; Mengyu, L.; Horinek, D.; Netz, R. R. *J. Stat. Phys.* **2011**, *145*, 240–252.

(13) Chowdhary, J.; Ladanyi, B. M. *J. Phys. Chem. B* **2009**, *113*, 4045–4053.

(14) Liu, P.; Harder, E.; Berne, B. J. *J. Phys. Chem. B* **2005**, *109*, 2949–2955.

(15) Fábián, B.; Senćanski, M. V.; Cvijetić, I. N.; Jedlovszky, P.; Horvai, G. *J. Phys. Chem. C* **2016**, *120*, 8578–8588.

(16) Milischuk, A. A.; Ladanyi, B. M. *J. Chem. Phys.* **2011**, *135*, 174709.

(17) Jiao, S.; Xu, Z. *ACS Nano* **2017**, *11*, 11152–11161.

(18) Faraone, A.; Fratini, E.; Todea, A. M.; Krebs, B.; Müller, A.; Baglioni, P. *J. Phys. Chem. C* **2009**, *113*, 8635–8644.

(19) Mitra, T.; Miró, P.; Tomsa, A.-R.; Merca, A.; Bögge, H.; Ávalos, J.; Poblet, J. M.; Bo, C.; Müller, A. *Chem. Eur. J.* **2009**, *115*, 1844–1852.

(20) Garcia-Ratés, M.; Miró, P.; Poblet, J. M.; Bo, C.; Avalos, J. B. *J. Phys. Chem. B* **2011**, *19*, 5980–5992.

(21) Garcia-Ratés, M.; Miró, P.; Müller, A.; Bo, C.; Avalos, J. B. *J. Phys. Chem. C* **2014**, *118*, 5545–5555.

(22) Cringus, D.; Lindner, J.; Milder, M. T. W.; Pshenichnikov, M. S.; Vöhringer, P.; Wiersma, D. A. *Chem. Phys. Lett.* **2005**, *408*, 162–168.

(23) Cringus, D.; Bakulin, A.; Lindner, J.; Vöhringer, P.; Pshenichnikov, M. S.; Wiersma, D. A. *J. Phys. Chem. B* **2007**, *111*, 14193–14207.

(24) Fayer, M. D. *Acc. Chem. Res.* **2012**, *45*, 3–14.

(25) Moilanen, D. E.; Levinger, N. E.; Spry, D. B.; Fayer, M. D. *J. Am. Chem. Soc.* **2007**, *129*, 14311–14318.

(26) Park, S.; Moilanen, D. E.; Fayer, M. D. *J. Phys. Chem. B* **2008**, *112*, 5279–5290.

(27) van der Loop, T. H.; Ottosson, N.; Lotze, S.; Kentzinger, E.; Vad, T.; Sager, W. F. C.; Bakker, H. J.; Woutersen, S. *J. Chem. Phys.* **2014**, *141*, 535.

(28) Faeder, J.; Ladanyi, B. M. *J. Phys. Chem. B* **2000**, *104*, 1033–1046.

(29) Rosenfeld, D. E.; Schmuttenmaer, C. A. *J. Phys. Chem. B* **2011**, *115*, 1021–1031.

(30) Ghysels, A.; Venable, R. M.; Pastor, R. W.; Hummer, G. *J. Chem. Theory Comput.* **2017**, *13*, 2962–2976.

(31) Luzar, A.; Chandler, D. *Nature* **1996**, *379*, 55–57.

(32) Luzar, A. *J. Chem. Phys.* **2000**, *113*, 10663.

(33) Berendsen, H. J. C.; Grigera, J. R.; Straatsma, T. P. *J. Phys. Chem.* **1987**, *91*, 6269–6271.

(34) Daub, C. D.; Wang, J.; Kudesia, S.; Bratko, D.; Luzar, A. *Faraday Discuss.* **2010**, *146*, 67–77.

(35) von Domaros, M.; Bratko, D.; Kirchner, B.; Luzar, A. *J. Phys. Chem. C* **2013**, *117*, 4561–4567.

(36) Choudhuri, J. R.; Vanzo, D.; Madden, P. A.; Salanne, M.; Bratko, D.; Luzar, A. *ACS Nano* **2016**, *10*, 8536–8544.

(37) Ojaghlou, N.; Tafreshi, H.; Bratko, D.; Luzar, A. *Soft Matt.* **2018**, *14*, 8924–8934.

(38) Daub, C. D.; Cann, N. M.; Bratko, D.; Luzar, A. *Phys. Chem. Chem. Phys.* **2019**, *20*, 27838–27848.

(39) Lamoureux, G.; Harder, E.; Vorobyov, I.; MacKerell, A. D. *Chem. Phys. Lett.* **2006**, *418*, 245–249.

(40) Kiss, P. T.; Baranyai, A. *J. Chem. Phys.* **2006**, *418*, 204507.

(41) Shafiei, M.; von Domaros, M.; Bratko, D.; Luzar, A. *J. Chem. Phys.* **2019**, *150*, doi: 10.1063/1.5079393.

(42) Schwerdtfeger, P.; Wirz, L.; Avery, J. *J. Comput. Chem.* **2013**, *34*, 1508–1526.

(43) Werder, T.; Walther, J. H.; Jaffe, R. L.; Halicioglu, T.; Koumoutsakos, P. *J. Phys. Chem. B* **2003**, *107*, 1345–1352.

(44) Shin, S.; Willard, A. P. *J. Phys. Chem. B* **2018**, *122*, 6781–6789.

(45) Vaitheeswaran, S.; Yin, H.; Rasaiah, J. C.; Hummer, G. *Proc. Natl. Acad. Sci.* **2004**, *101*, 17002–17005.

(46) Bratko, D.; Curtis, R. A.; Blanch, H. W.; Prausnitz, J. M. *J. Chem. Phys.* **2001**, *115*, 3873–3877.

(47) Bratko, D.; Daub, C. D.; Leung, K.; Luzar, A. *J. Am. Chem. Soc.* **2007**, *129*, 2504–2510.

(48) Plimpton, S. *J. Comput. Phys.* **1995**, *117*, 1–19.

(49) Mittal, J.; Hummer, G. *J. Chem. Phys.* **2012-07**, *137*, 034110.

(50) Hummer, G. *New J. Phys.* **2005**, *7*, 34.

(51) Sriraman, S.; Kevrekidis, I. G.; Hummer, G. *J. Phys. Chem. B* **2005**, *109*, 6479–6484.

(52) Phan, A.; Cole, D. R.; Weiss, R. G.; Dzubiella, J.; Striolo, A. *ACS Nano* **2016**, *10*, 7646–7656.

(53) Kayal, A.; Chandra, A. *Mol. Simul.* **2015**, *41*, 463–470.

(54) Benjamin, I. *Reviews in Computational Chemistry*; John Wiley & Sons, Inc, 2015; Vol. 28; pp 205–313.

(55) Yeh, I.-C.; Hummer, G. *J. Phys. Chem. B* **2004**, *108*, 15873–15879.

(56) Tazi, S.; Boţan, A.; Salanne, M.; Marry, V.; Turq, P.; Rotenberg, B. *J. Phys. Condens. Matter* **2012**, *24*, 284117.

(57) Weiß, R. G.; Heyden, M.; Dzubiella, J. *Phys. Rev. Lett.* **2015**, *114*, 19–21.

(58) Luzar, A. *Faraday Discuss.* **1996**, *103*, 29–40.

Graphical TOC Entry

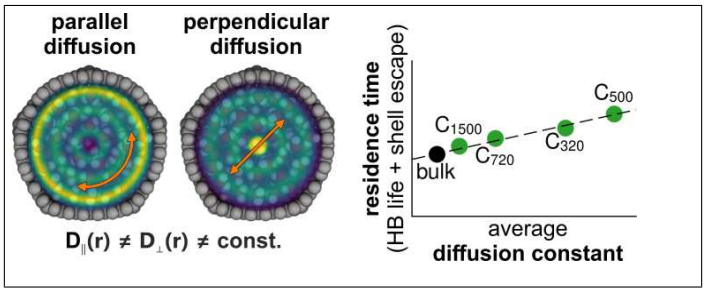

Supporting Information: Multifaceted Water Dynamics in Spherical Nanocages

Michael von Domaros,[†] Dusan Bratko,[‡] Barbara Kirchner,[¶] Gerhard Hummer,[§] and Alenka Luzar[*,‡]

†*Department of Chemistry, University of California, Irvine, Irvine, CA 92697, USA*
‡*Department of Chemistry, Virginia Commonwealth University, Richmond, VA 23284, USA*
¶*Mulliken Center for Theoretical Chemistry, University of Bonn, 53127 Bonn, Germany*
§*Max Planck Institute of Biophysics, 60438 Frankfurt am Main, Germany*

E-mail: aluzar@vcu.edu

Water Network Structure

For the lack of specialized metrics of hydrogen bond structure in anisotropic environments, we rely on hydrogen-bond criteria and a tetrahedral order parameter originally developed for isotropic systems. Similar approximations have proven to yield useful insights into structural properties of hydration water[1] The order parameter we use is split into an angular (S_g) and distance (S_k) part, according to the definition[2] of Chau and Hardwick:

$$S_g = \frac{3}{32} \sum_{j=1}^{3} \sum_{k=j+1}^{4} \left(\cos \Psi_{j,k} + \frac{1}{3} \right)^2 \tag{S1}$$

$$S_k = \frac{1}{3} \sum_{k=1}^{4} \frac{\left(r_k - \hat{r}\right)^2}{4\hat{r}^2} \,. \tag{S2}$$

Therein, the summation indices run over the four closest neighbors of a selected water molecule, $\Psi_{j,k}$ denotes the angle between the central molecule and its neighbors j and k, r_k is the distance to the closest neighbor k, and $\hat{r}$ is the arithmetic mean of the four radial distances. Both values are zero for a perfect tetrahedron, but approach somewhat larger values ($S_g \approx 0.1, S_k \approx 1.3 \times 10^{-3}$) in bulk water at ambient conditions.[2] The parameters are shown in Figures S1 and S2 and their discussion follows shortly.

Hydrogen bonds were detected by the same geometric criterion used in the discussion of hydrogen bond kinetics[3,4] (main article). The ensemble average of the hydrogen bond population operator $\langle h \rangle$ is closely related to the average number of hydrogen bonds per water molecule $\langle n_{\mathrm{hb}} \rangle$, according to

$$\langle n_{\mathrm{hb}} \rangle = \frac{N-1}{2} \langle h \rangle \,. \tag{S3}$$

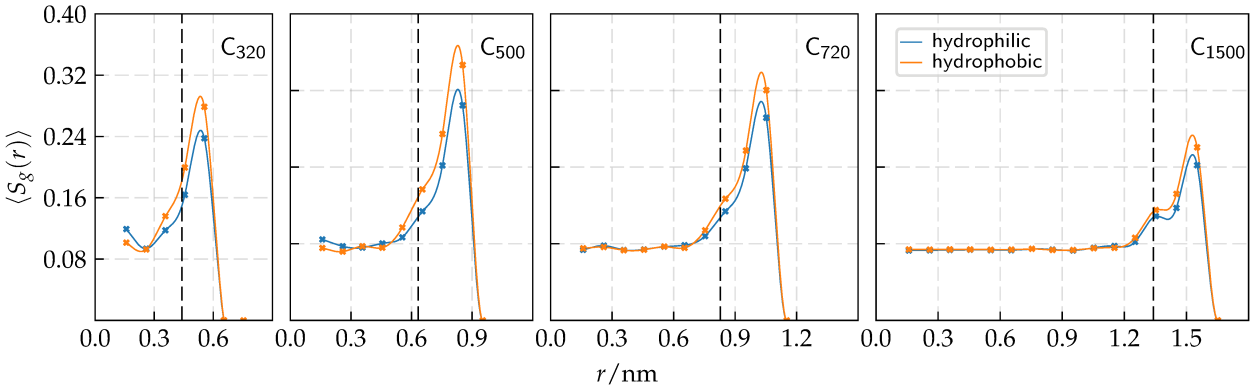

Figure S1: Average angular part $\langle S_g\,(r)\rangle$ of the tetrahedral order parameter[2] as a function of the radial distance r from the nanocage center. Lines are meant to guide the eye. The dashed vertical line indicates the position of the interfacial density maximum.

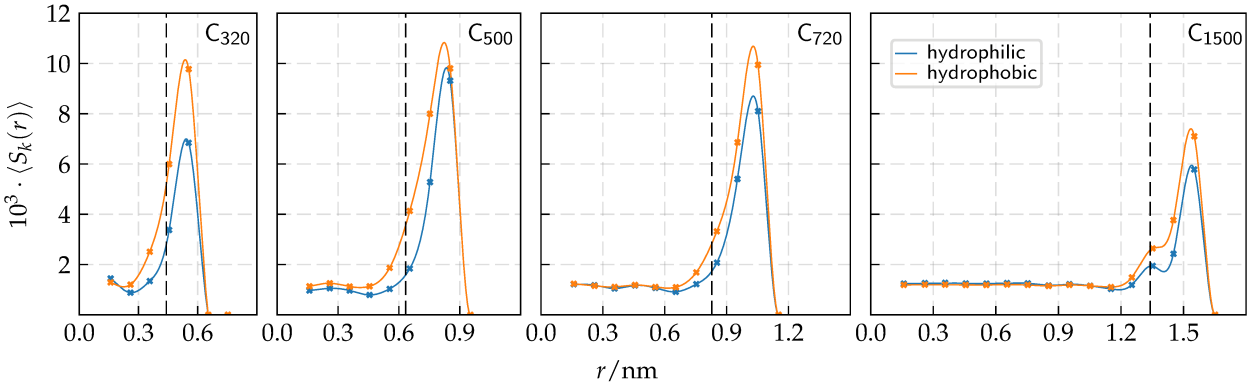

Figure S2: Average of the distance part $\langle S_k\,(r)\rangle$ of the tetrahedral order parameter[2] as a function of the radial distance r from the nanocage center. Lines are meant to guide the eye. The dashed vertical line indicates the position of the interfacial density maximum.

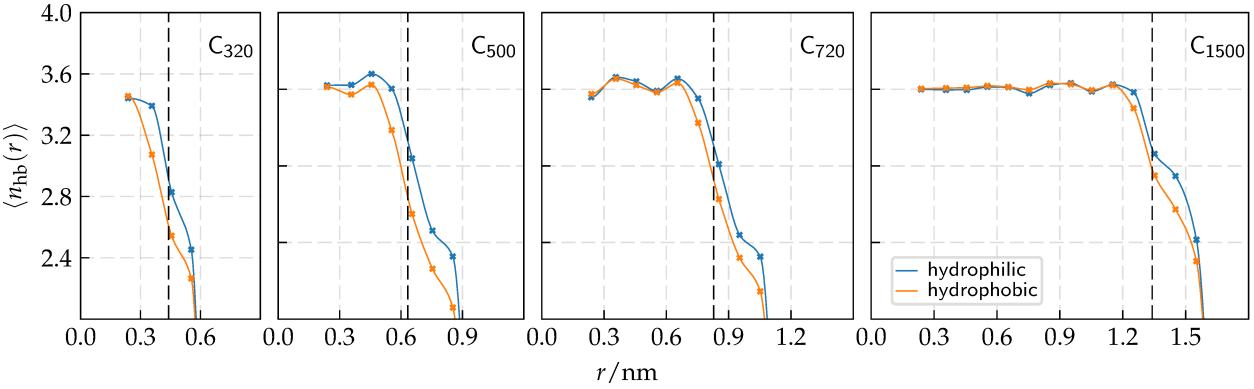

Figure S3: Average number of hydrogen bonds per water molecule $\langle n_{\mathrm{hb}}\,(r)\rangle$ as a function of the radial distance r from the nanocage center. Lines are meant to guide the eye. The dashed vertical line indicates the position of the interfacial density maximum.

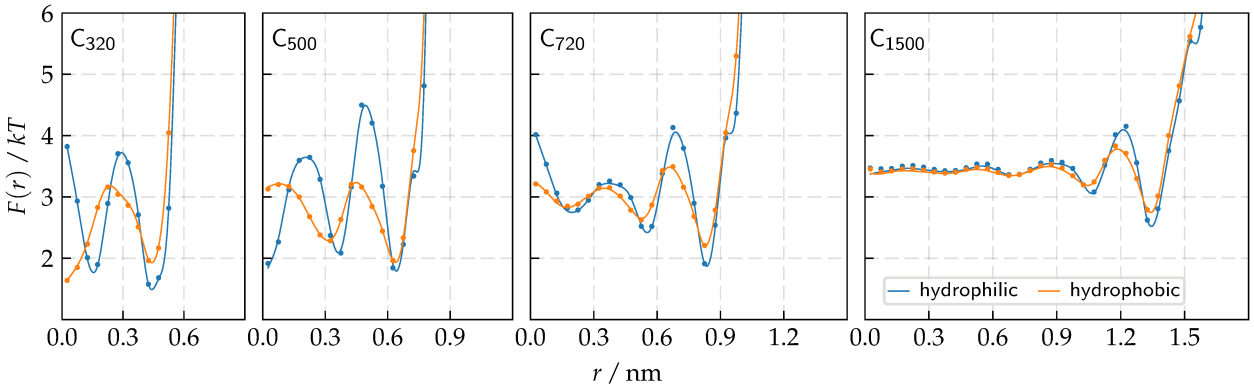

Figure S4: Free energy profiles $F(r)$ as a function of the radial distance r from the nanocage center. Results were obtained from counting statistics (solid lines) and from Bayesian sampling (dots).

Distance dependent profiles of these averages are shown in Figure S3.

The profiles shown in Figures S1–S3 report on the water hydrogen bond network in one way or another, and thus, share a number of common features. In all systems, the interfacial hydrogen bond network is being significantly disturbed by the interface. The average number of hydrogen bonds is almost halved within the outermost water shell, which is accompanied by significant distortion of tetrahedrality. These effects are more pronounced in hydrophobic than in hydrophilic cages. Water molecules that reside away from the outermost water shell are less hindered by the geometric restrictions, as indicated by the plateau values of the various parameters.

Diffusion

Note that free energy profiles are also directly accessible from counting statistics

$$F(r) = -kT \ln p(r), \tag{S4}$$

where $p(r)$ is the local probability density of finding a particle at position r. The preceding equation can be evaluated by discretization and results are shown in comparison to those obtained from the Bayesian sampling procedure in Figure S4. Agreement is perfect, further increasing the confidence in our diffusion models.

The radial and angular propagators $G(r, t|r', 0)$ and $P(r, \cos\theta, t|r', 0)$ corresponding to those in the main text, but in the hydrophilic confinements, are shown in Figure S5. They behave qualitatively as their hydrophobic counterparts.

Furthermore, we show additional angular propagators $P(r, \cos\theta, t|r', 0)$ where r' has been restricted to the outermost radial density minimum $r_{\min}$ (Figure S6). In combination with those propagators shown for the interfacial density maximum, the data shown here and in the main text covers the most critical regions of our systems. Once again, agreement between model and simulation data is less perfect in angular than in radial direction, but still quantitatively convincing.

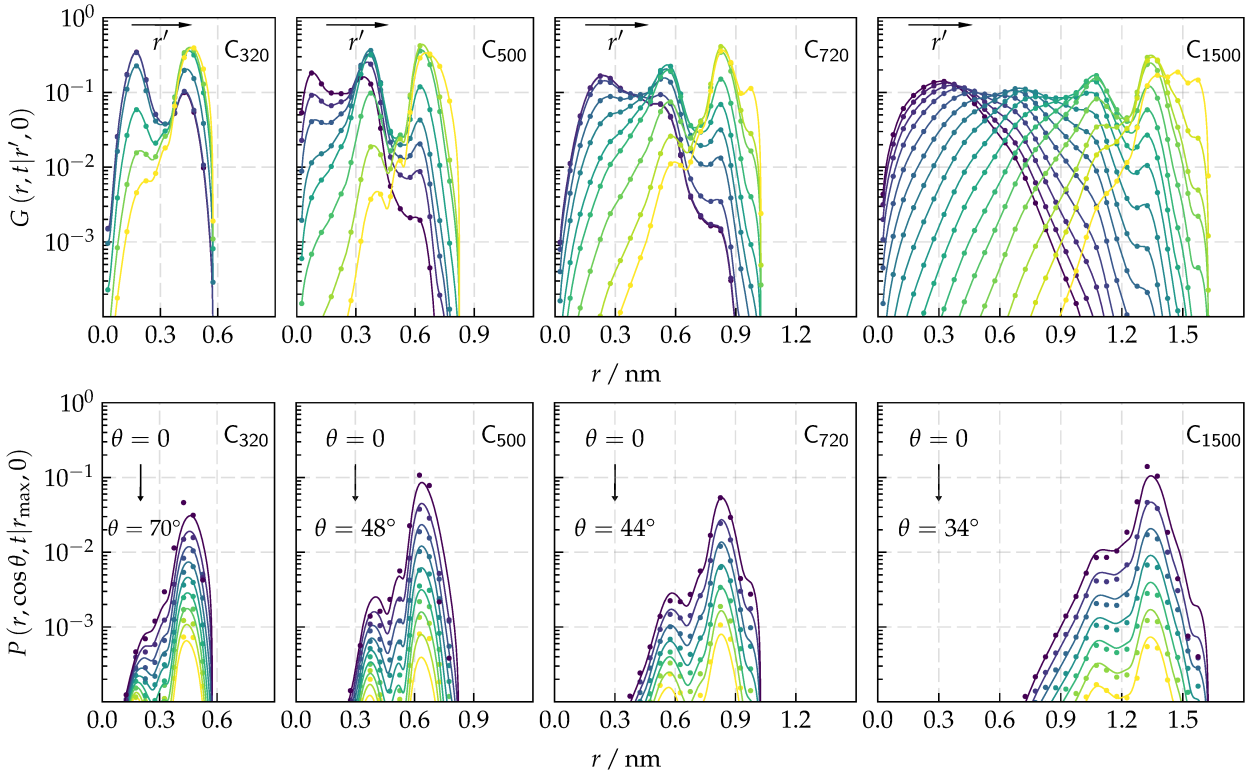

Figure S5: Model propagators (solid lines) in radial and angular direction, $G\,(r,t|r',0)$ and $P\,(r,\cos\theta,t|r',0)$, compared to simulation data (symbols) in the hydrophilic confinements for a lag time of 10 ps. The color gradient indicates increasing initial positions r' and $\cos\theta$, respectively.

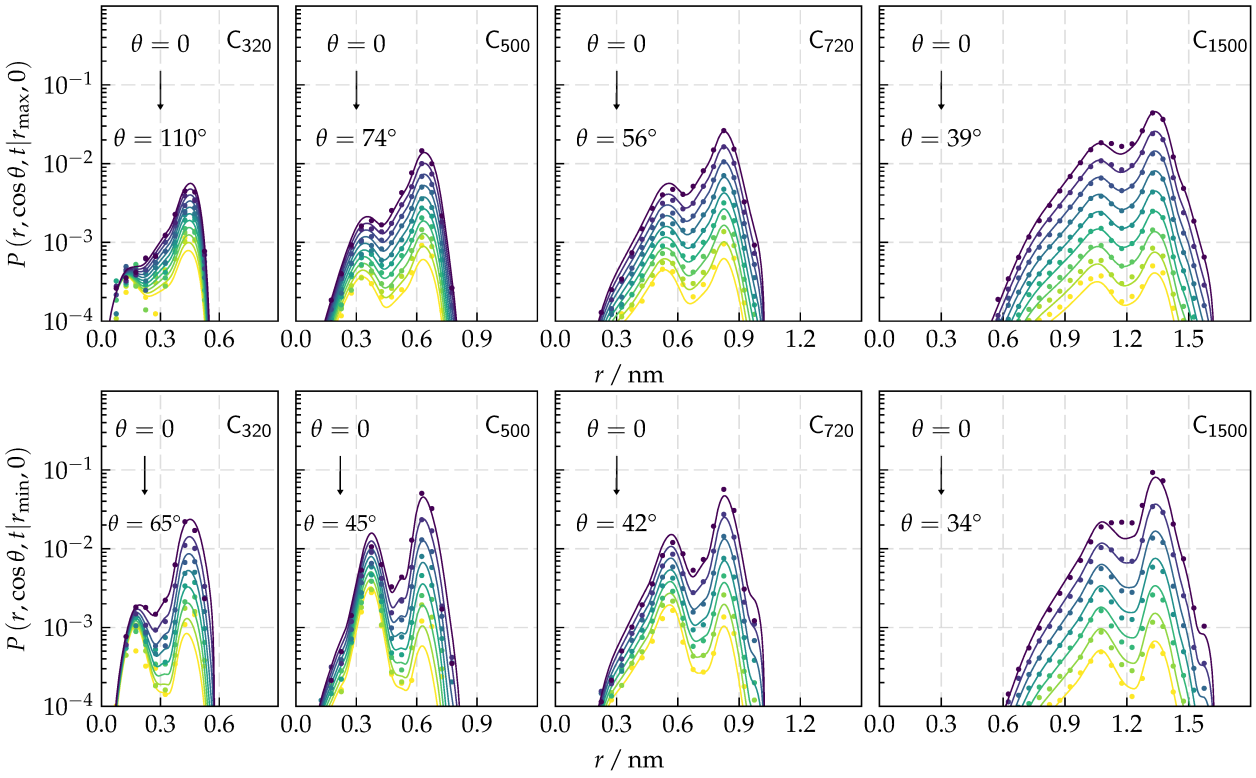

Figure S6: Model propagators $P\,(r, \cos\theta, t|r', 0)$ (solid lines) compared to simulation data (symbols) in the hydrophobic confinements (top) and hydrophilic confinements (bottom) for a lag time of 10 ps. The initial position of the particle has been restricted to the outermost density minimum $r' = r_{\mathrm{min}}$ in this plot. The color gradient indicates decreasing values of $\cos\theta$.

We observe a non-monotonic dependence of the interfacial diffusivities $D_\perp(R_\mathrm{G})$ and $D_\parallel(R_\mathrm{G})$ (Fig. S7), where R_G is the approximate location of the Gibbs dividing surface defined in analogy to ref. 5. Although the curves are reminiscent of those observed at convex interfaces,[5] where the minimum has been explained with the structural crossover length scale for hydrophobic hydration, the underlying mechanisms cannot be the same, since there is no such crossover in our systems.

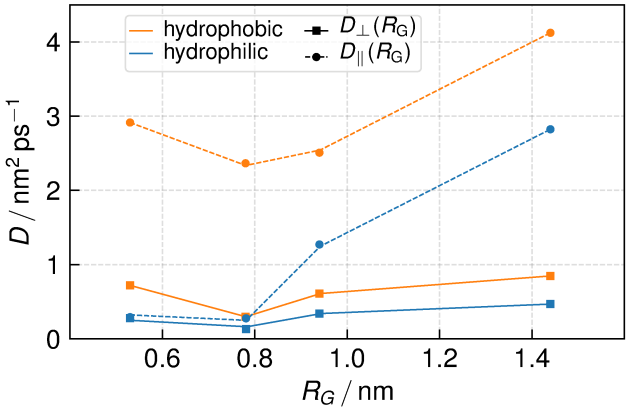

Figure S7: Interfacial diffusivities $D_\perp(R_\mathrm{G})$ and $D_\parallel(R_\mathrm{G})$ at the approximate location of the Gibbs dividing surface (i.e., where $\rho(R_\mathrm{G}) \sim {}^1\!/_2\,\rho_\mathrm{bulk}$). Lines are meant to guide the eye.

Hydrogen Bond Kinetics

Here, we show reactive flux time correlation functions $k(t)$ and $k_\mathrm{in}(t)$, as well as their model predictions, and correlation plots for bulk water (Figure S8), for the hydrophobic confinements (Figure S9), and for the hydrophilic confinements (Figure S10). All parameters required in our analyses are summarized in Table S1. A discussion of these results has been given in the main text.

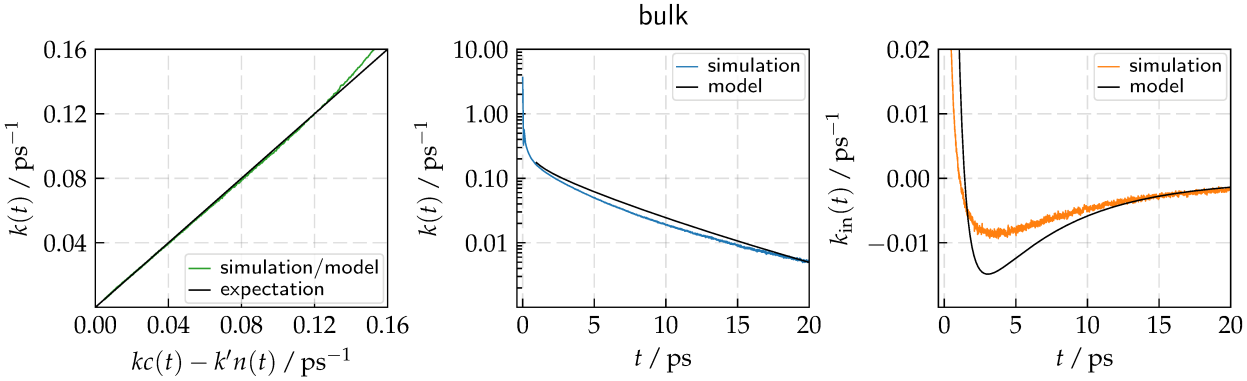

Figure S8: Correlation between the hydrogen bond kinetics phenomenology and simulation data, as well as the reactive flux time correlation functions $k(t)$ and $k_\mathrm{in}(t)$ and their respective model predictions (Equation (6); main text) in bulk SPC/E water.

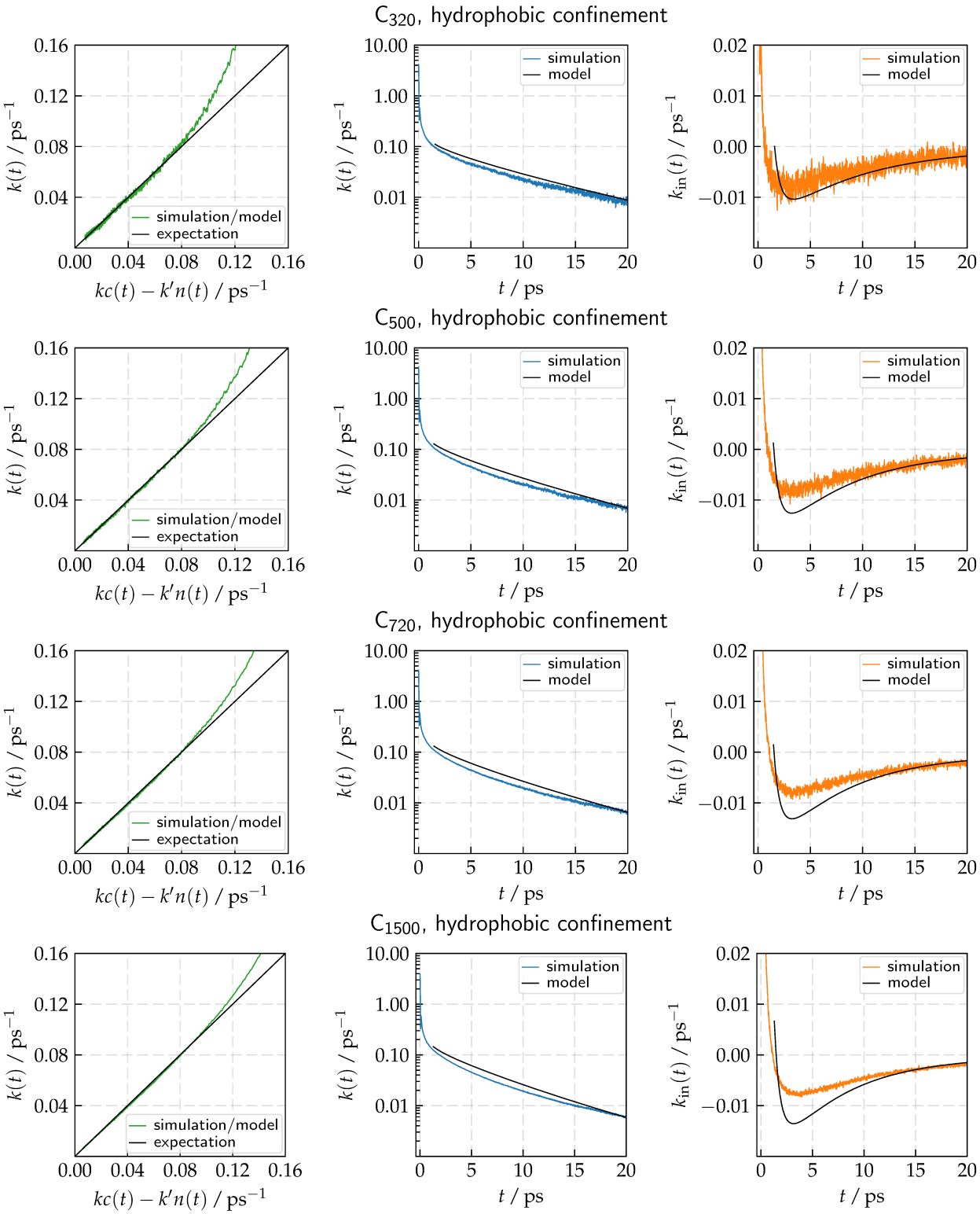

Figure S9: Correlation between the hydrogen bond kinetics phenomenology and simulation data, as well as the reactive flux time correlation functions $k(t)$ and $k_{\mathrm{in}}(t)$ and their respective model predictions (Equation (6); main text) in all hydrophobic confinements.

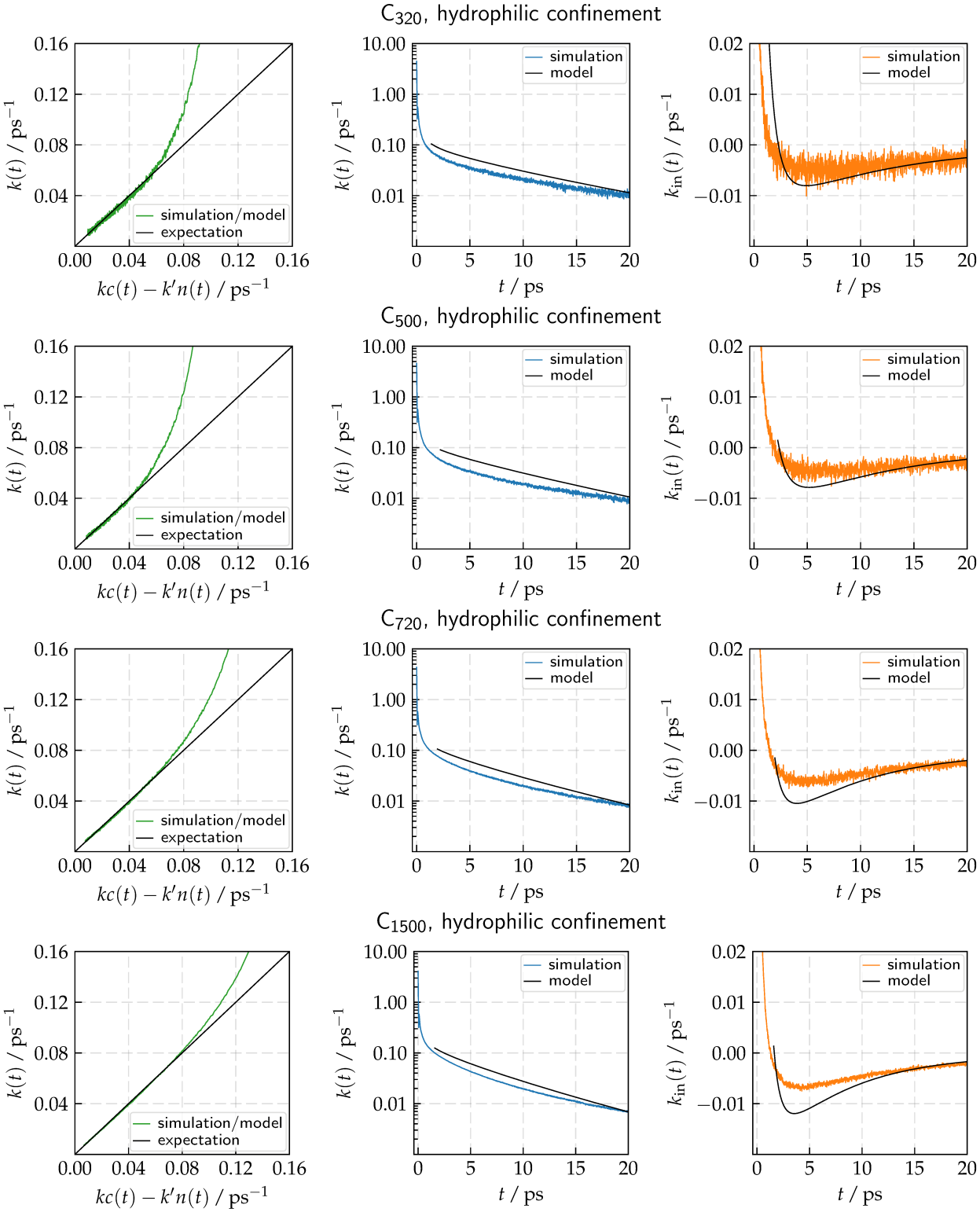

Figure S10: Correlation between the hydrogen bond kinetics phenomenology and simulation data, as well as the reactive flux time correlation functions $k(t)$ and $k_{\mathrm{in}}(t)$ and their respective model predictions (Equation (6); main text) in all hydrophilic confinements.

Table S1: Forward and backward rate constants k and k' (in units of ps^{-1}), describing the hydrogen bond kinetics, as well as diffusive time scales τ_d and hydrogen bond lifetimes $\tau_\mathrm{hb} = 1/k$ (in units of ps). Note that both k and k' can be varied by $\approx 10\,\%$, while still leading to acceptable model fits. Bulk values are $k = 0.35\,\mathrm{ps}^{-1}$, $k' = 0.72\,\mathrm{ps}^{-1}$, $\tau_\mathrm{d} = 0.46\,\mathrm{ps}$, and $\tau_\mathrm{hb} = 2.90\,\mathrm{ps}^{-1}$.

	hydrophilic				hydrophobic			
	k	k'	τ_d	τ_hb	k	k'	τ_d	τ_hb
C_{320}	0.21	0.54	0.77	4.76	0.30	0.89	0.56	3.33
C_{500}	0.19	0.40	0.66	5.26	0.33	0.82	0.52	3.08
C_{720}	0.26	0.57	0.59	3.92	0.33	0.76	0.52	3.08
C_{1500}	0.29	0.65	0.52	3.45	0.33	0.75	0.48	3.03

References

(1) Soper, A. K.; Castner, E. W.; Luzar, A. Impact of Urea on Water Structure: A Clue to its Properties as a Denaturant? *Biophys. Chem.* **2003**, *105*, 649–666.

(2) Chau, P.-L.; Hardwick, A. J. A New Order Parameter for Tetrahedral Configurations. *Mol. Phys.* **1998**, *93*, 511–518.

(3) Luzar, A.; Chandler, D. Hydrogen-Bond Kinetics in Liquid Water. *Nature* **1996**, *379*, 55–57.

(4) Luzar, A. Resolving the Hydrogen Bond Dynamics Conundrum. *J. Chem. Phys.* **2000**, *113*, 10663.

(5) Weiß, R. G.; Heyden, M.; Dzubiella, J. Curvature Dependence of Hydrophobic Hydration Dynamics. *Phys. Rev. Lett.* **2015**, *114*, 19–21.